

# NF-ULA: Langevin Monte Carlo with Normalizing Flow Prior for Imaging Inverse Problems

Ziruo Cai, Junqi Tang, Subhadip Mukherjee, Jinglai Li, Carola-Bibiane Schönlieb, and Xiaoqun Zhang

**Abstract**—Bayesian methods for solving inverse problems are a powerful alternative to classical methods since the Bayesian approach gives a probabilistic description of the problems and offers the ability to quantify the uncertainty in the solution. Meanwhile, solving inverse problems by data-driven techniques also proves to be successful, due to the increasing representation ability of data-based models. In this work, we try to incorporate the data-based models into a class of Langevin-based sampling algorithms in Bayesian inference. Loosely speaking, we introduce NF-ULA (Unadjusted Langevin algorithms by Normalizing Flows), which involves learning a *normalizing flow* as the prior. In particular, our algorithm only requires a pre-trained normalizing flow, which is independent of the considered inverse problem and the forward operator. We perform theoretical analysis by investigating the well-posedness of the Bayesian solution and the non-asymptotic convergence of the NF-ULA algorithm. The efficacy of the proposed NF-ULA algorithm is demonstrated in various imaging problems, including image deblurring, image inpainting, and limited-angle X-ray computed tomography (CT) reconstruction.

**Index Terms**—Bayesian inference, Langevin algorithms, normalizing flows, inverse problems.

## I. INTRODUCTION

Imaging inverse problems can be formulated as

$$y = A(x) + n,$$

where  $y \in \mathbb{R}^m$  is the indirect noisy observation,  $A : \mathbb{R}^d \rightarrow \mathbb{R}^m$  is the observation operator,  $n$  is the noise and  $x \in \mathbb{R}^d$  is the unknown original image that one aims to recover. Following the surge of deep learning, data-driven regularization methods have become ubiquitous in imaging inverse problems [1], [2], leading to state-of-the-art results which significantly outperform classical hand-crafted regularization schemes such as the total-variation [3]. Starting from the plug-and-play methods [4] which combine proximal-splitting optimization algorithms [5] with learned denoisers [6]–[8], researchers have made massive efforts on this direction. Current popular trends

in this line of research includes the studies in improving practical performances and theoretical guarantees [9]–[13], the developments of deep unrolling networks [14], the extension of generative models in imaging applications [15]–[18], and the works in learning explicitly the regularization functional such as the gradient-step denoiser [19], total deep variation [20], adversarial regularizers [21]–[23] and more recently the learned convex regularizer [24] with input-convex neural networks [25].

Another popular way of solving inverse problems is to do it in a Bayesian setting [26]–[28]. Different from the functional-analytic methods, Bayesian methods are trying to explore the posterior distribution  $p(x|y)$  based on some statistical techniques, e.g., Bayes’ formula. The methods based on Bayesian inference can not only give a statistical estimator, e.g., maximum a posteriori estimator, for the problem, but also describe the uncertainty in the solution in a probabilistic way, e.g., variance and credibility intervals. This is helpful to decision-making and reliability assessment. Typical examples of Bayesian imaging schemes include the classical approach by total variation prior [29], [30], and more recently by the patch-based models [31]–[34].

In Bayesian inference, one conventional method to explore the posterior distributions is to generate samples from them, such as the Markov Chain Monte Carlo (MCMC) methods [35]. Among those sampling algorithms, the Langevin Monte Carlo (LMC) algorithms [36], [37], also named Unadjusted Langevin Algorithms (ULA), stand out as an increasingly popular tool, due to its efficiency of exploring the state space. In recent years, the theoretical analysis and nonasymptotic convergence of ULA [38], [39] opened a new chapter for the studies of ULA. Except for convex and smooth potentials [38]–[41], ULA of other curvatures conditions have also shown great progress. While ULA requires evaluating the gradient of potentials, ULA for non-smooth distributions [30], [42]–[46] draw samples from a smoothed substitution, borrowing the proximity tools in non-smooth optimization. For non-convex potentials, ULA also have convergence guarantees [47]–[50], if some conditions on the drift is satisfied.

Incorporating data-based models into the algorithms is a trending topic of ULA. To be more specific, one aims to utilize an over-parameterized model learned on given data, such as neural network, instead of modeling the prior in the traditional way. Recently, Langevin Monte Carlo using Plug and Play Prior (PnP-ULA) [51] shows promising results on Bayesian imaging problems. It learns a Plug and Play Prior [4] by a Lipschitz imaging denoiser [52]. Since the original prior of given data is not assumed to be convex or smooth, PnP-ULA

Manuscript received \*\*\*\*\*, 2023; revised \*\*\*\*\*, 2023.

Z. Cai is with the School of Mathematical Sciences, Shanghai Jiao Tong University, China (e-mail: [sjtu\\_caiziruo@sjtu.edu.cn](mailto:sjtu_caiziruo@sjtu.edu.cn)).

J. Tang is with the School of Mathematics, University of Birmingham (email: [j.tang.2@bham.ac.uk](mailto:j.tang.2@bham.ac.uk)).

S. Mukherjee was with the Department of Applied Mathematics and Theoretical Physics, University of Cambridge, when this work was being undertaken (email: [subhadipju@gmail.com](mailto:subhadipju@gmail.com)).

J. Li is with the School of Mathematics, University of Birmingham (email: [j.li.10@bham.ac.uk](mailto:j.li.10@bham.ac.uk)).

C. Schönlieb is with the Department of Applied Mathematics and Theoretical Physics, University of Cambridge (email: [cbs31@cam.ac.uk](mailto:cbs31@cam.ac.uk)).

X. Zhang is with the School of Mathematical Sciences, MOELSC and Institute of Natural Sciences, Shanghai Jiao Tong University, Shanghai 200040, China (e-mail: [xqzhang@sjtu.edu.cn](mailto:xqzhang@sjtu.edu.cn)).

is actually an ULA with non-convex potentials.

Except for Plug and Play Prior [4], Normalizing Flows (NF) [53]–[55] also show great performance on imaging problems [54], [56] and have potential of serving as the prior in the Bayesian imaging framework. In this work, we try to integrate a prior learned by NF into the Langevin algorithms. Therefore the potential we learned is also non-convex. To make the model well-defined in the Bayesian settings and make the algorithm numerically stable, we follow PnP-ULA [51] to make minor changes to the standard ULA.

**Our contributions:** We propose NF-ULA, a novel framework of sampling by Langevin Monte Carlo based algorithms, while leveraging a pre-trained normalizing flow induced prior. We proved that the Bayesian solutions are well-defined and well-posed. We give a sufficient condition to ensure the Lipschitz gradient of the log distribution of the normalizing flows. We establish the convergence analysis of NF-ULA, that is, NF-ULA admits an invariant distribution. We give a nonasymptotic bound of bias. We demonstrate that our proposed approach yields high-quality results by experiments such as image deblurring, image inpainting and limited-angle computed tomography reconstruction. We also provide evidence that enhanced training of the normalizing flows implies an improved sampling and reconstruction.

The rest of the paper is organized as follows: Sec. II gives a brief review of both Langevin Monte Carlo and normalizing flow, then introduces NF-ULA. Sec. III is the theoretical analysis about the Bayesian solution and NF-ULA. In Sec. IV, we evaluate NF-ULA on image deblurring, image inpainting and limited-angle CT reconstruction. Final conclusions are summarized in Sec. V.

## II. PROBLEM SETUP

In this section, we give some background on Langevin Monte Carlo (LMC) algorithms and normalizing flow. Then we propose NF-ULA, an LMC algorithm that takes advantage of a pre-trained normalizing flow network.

### A. LMC for Non-smooth Potentials

In Bayesian inference, there is a broad class of problems where we aim to draw samples  $\{X_k\}_{k=1}^K, X_k \in \mathbb{R}^d$ , from the distribution  $p(x|y)$ , given the observation  $y \in \mathbb{R}^m$ . Using Bayes' formula, we have that

$$p(x|y) = \frac{p(y|x)p(x)}{\int p(y|\tilde{x})p(\tilde{x})d\tilde{x}}. \quad (1)$$

The well-known LMC approach [36], [37], also referred to as the *unadjusted Langevin algorithm* (ULA), is capable of efficient sampling from  $p(x|y)$ :

$$\begin{aligned} X_{k+1} &= X_k + \delta \nabla \log p(X_k|y) + \sqrt{2\delta} Z_{k+1} \\ &= X_k + \delta \nabla \log p(y|X_k) + \delta \nabla \log p(X_k) + \sqrt{2\delta} Z_{k+1}, \end{aligned} \quad (2)$$

where  $\{Z_k\}_k \sim \mathcal{N}(0, I^d)$  is a family of i.i.d. Gaussian random variables. ULA (2) is based on the Euler-Maruyama (EM) discretization of the over-damped Langevin Stochastic Differential Equation (SDE)

$$dX_t = \nabla \log p(X_t|y) dt + \sqrt{2} dB_t.$$

Provided that  $-\log p(x|y)$  is convex and continuously differentiable, the convergence of ULA can be guaranteed [38], [39], although subject to a bias related to the step-size  $\delta$ . In general, smaller  $\delta$  leads to a smaller bias and larger  $\delta$  leads to faster convergence of the Markov Chain. To the best of our knowledge, the non-asymptotic bias and convergence analysis of ULA has remained relatively under-explored until the last few years [38]–[41]. Notably, the bias of ULA (2) can be removed by adding a Metropolis-Hasting (MH) accept-reject step, leading to the Metropolis-adjusted Langevin algorithm (MALA) [37]. In this paper, we will focus on the ULA without any MH adjustments.

When the potential  $-\log p(x)$  is convex but non-smooth, [42] studies the case where the Moreau envelope  $U^{(\lambda)}(x)$  of  $U(x) = -\log p(x)$  is used in (2). The definition of the Moreau envelope  $U^{(\lambda)}(x)$  and the proximity operator  $\text{prox}_{\lambda, U}$  is given by

$$\begin{aligned} U^{(\lambda)}(x) &:= \inf_{u \in \mathbb{R}^d} \left( U(u) + \frac{1}{2\lambda} \|x - u\|_2^2 \right). \\ \text{prox}_{\lambda, U}(x) &:= \arg \min_{u \in \mathbb{R}^d} \left( U(u) + \frac{1}{2\lambda} \|x - u\|_2^2 \right) \end{aligned}$$

Since the Moreau envelope  $U^{(\lambda)}(x)$  is always continuously differentiable [57], [58] even if  $U(x)$  is not, the authors of [42] replace  $\nabla \log p(x)$  by  $-\nabla U^{(\lambda)}(x) = (\text{prox}_{\lambda, U}(x) - x) / \lambda$  and propose Moreau-Yoshida regularized ULA (referred to as MYULA), which requires the proximal operator of  $U(x)$  in each iteration of (2).

In a more general case where the prior  $p(x)$  is not available in an explicit form, the authors of [51] propose a plug-and-play (PnP) approach to learn the prior [4], [52]. This is achieved by training a Lipschitz-continuous denoiser  $D_\varepsilon(x)$ . More precisely, the denoiser  $D_\varepsilon(x)$  is learned on a given dataset  $\{x_n\}_{n=1}^N$  by adding Gaussian noise of zero-mean and  $\varepsilon$  variance, where each  $x_n$  is assumed to be drawn i.i.d. from  $p(x)$ . Then the noisy data follows the smoothed prior

$$p_\varepsilon(x) = (2\pi\varepsilon)^{-d/2} \int_{\mathbb{R}^d} \exp[-\|x - \tilde{x}\|_2^2 / (2\varepsilon)] p(\tilde{x}) d\tilde{x},$$

which is the convolution of the non-explicit prior  $p(x)$  with a Gaussian smoothing kernel. Similar to the Moreau envelope [57], [58],  $p_\varepsilon$  is always differentiable and satisfies Tweedie's identity [59]:

$$\varepsilon \nabla \log p_\varepsilon(x) = D_\varepsilon(x) - x.$$

While computing  $\nabla \log p(x)$  is intractable, one can use  $\nabla \log p_\varepsilon(x)$  as a surrogate in (2), leading to the PnP-ULA approach [51]:

$$\begin{aligned} \text{(PnP-ULA)} : \quad X_{k+1} &= X_k + \delta \nabla \log p(y|X_k) \\ &+ \frac{\delta\alpha}{\varepsilon} (D_\varepsilon(X_k) - X_k) + \frac{\delta}{\lambda} (\Pi_C(X_k) - X_k) + \sqrt{2\delta} Z_{k+1}, \end{aligned} \quad (3)$$

where  $\alpha$  is a regularization parameter associated with the PnP prior and  $\{Z_k\}_k$  are i.i.d. drawn from  $\mathcal{N}(0, I^d)$ . A projection  $\Pi_C(X_k)$  onto a convex and compact set  $C$  is added in each iteration to ensure the stability of PnP-ULA. Moreover, the Lipschitz continuity of the denoiser  $D_\varepsilon(x)$  is required

for convergence. The detailed convergence analysis of (3) is available in [51].

### B. Normalizing Flow

A flow-based model seeks to express  $x \in \mathbb{R}^d$  as

$$x = T(z), \quad (4)$$

a transformation  $T$  of  $z \in \mathbb{R}^d$ ,  $z \sim q_z(z)$ . Here,  $q_z(z)$  is the base distribution of the flow-based model and is generally chosen to be a distribution that can be sampled easily, such as a multivariate Gaussian. The transformation  $T : \mathbb{R}^d \mapsto \mathbb{R}^d$  is invertible and both  $T$  and  $T^{-1}$  must be differentiable [53], [55]. The flow-based model is also called *normalizing flow*, since  $T^{-1}$  implicitly transforms  $q(x)$  into a normal distribution. In practice,  $T$  is typically implemented with an invertible neural network [54], [56]. By a change of variables in (4), the distribution of  $x$  is given by

$$\begin{aligned} q(x) &= q_z(z) |\det J_T(z)|^{-1} \\ &= q_z(T^{-1}(x)) |\det J_{T^{-1}}(x)|, \end{aligned} \quad (5)$$

where  $z = T^{-1}(x)$  and the Jacobian  $J_T(z)$  is the  $d \times d$  matrix

$$J_T(z) = \begin{bmatrix} \frac{\partial T_1}{\partial z_1} & \cdots & \frac{\partial T_1}{\partial z_d} \\ \vdots & \ddots & \vdots \\ \frac{\partial T_d}{\partial z_1} & \cdots & \frac{\partial T_d}{\partial z_d} \end{bmatrix}.$$

Many normalizing flows [55] use specific network architectures such that the Jacobian  $J_{T^{-1}}(x)$  is a triangular matrix function and then  $T^{-1}$  is called a triangular mapping. Note that  $T$  is used when sampling  $x$  from  $z$ , and  $T^{-1}$  is needed when evaluating the density  $q(x)$ .

As we introduced in Sec. II-A, assume that the unknown prior distribution we aim to learn is  $p(x)$ . Then, the forward KL divergence between the target distribution  $p(x)$  and the output distribution  $q(x)$  of the NF model can be written as

$$\begin{aligned} D_{\text{KL}}(p, q) &= -\mathbb{E}_{p(x)} [\log q(x)] + \text{const.} \\ &= -\mathbb{E}_{p(x)} [\log q_z(T^{-1}(z)) + \log |\det J_{T^{-1}}(x)|] + \text{const.} \end{aligned} \quad (6)$$

In fact, when the transformation  $T$  is parameterized by an invertible neural network  $T_\theta$  with parameters  $\theta \in \Theta$ , we denote the parameterized density of  $x$  as  $q_\theta(x)$  and the optimization problem of learning  $T_\theta$  and  $q_\theta$  is formulated as:

$$\min_{\theta \in \Theta} D_{\text{KL}}(p, q_\theta). \quad (7)$$

Assume that we have a set of samples  $\{x_n\}_{n=1}^N$  drawn i.i.d. from  $p(x)$ , we can estimate the expectation in (6) over  $p(x)$  by Monte Carlo averaging, as the mean value over the samples  $\{x_n\}_{n=1}^N$ . Correspondingly, the loss function for training the NF model becomes

$$\mathcal{L}(\theta) = -\frac{1}{N} \sum_{i=1}^N \log q_\theta(x_i) + \text{const.} \quad (8)$$

Generally, it is reasonable to assume that the data samples  $\{x_i\}_i^N$  lie within a compact set  $C_R \subset \mathbb{R}^d$ . In particular, when the flow-based model is learned on imaging data, it is common to set  $C_R = [0, 1]^d$ .

### C. ULA by NF-prior

In this section, we propose a framework of sampling by the LMC algorithm based on a pre-trained normalizing flow network. Given data samples  $\{x_k\}_{k=1}^N$  drawn i.i.d. drawn from  $p(x)$ , one can approximate the distribution  $p(x)$  by learning a flow-based model  $x = T_\theta(z)$ , with output distribution  $q_\theta(x) = q_z(T_\theta^{-1}(x)) |\det J_{T_\theta^{-1}}(x)|$ . Once  $q_\theta(x)$  is learned by the normalizing flow,  $\log q_\theta(x)$  is always differentiable since  $T_\theta$  and  $T_\theta^{-1}$  are differentiable. By replacing  $p(x)$  with  $q_\theta(x)$  in (2), the ULA scheme boils down to

$$X_{k+1} = X_k + \delta \nabla \log p(y|X_k) + \delta \nabla \log q_\theta(X_k) + \sqrt{2\delta} Z_{k+1}.$$

Since the convexity and Lipschitz gradient of  $-\log q_\theta(x)$  are not known to be satisfied, one cannot immediately infer convergence and the numerical stability similar to the cases in [38], [39]. In this work, we follow [51] to impose a projection  $\Pi_C(X_k)$  onto a convex and compact set  $C$  to ensure that the posterior distribution is well-defined, and propose NF-ULA (c.f. Algorithm 1).

---

#### Algorithm 1 NF-ULA

---

Input:  $y \in \mathbb{R}^m$ ,  $X_0 \in \mathbb{R}^d$ ,  $\alpha > 0$ ,  $\lambda > 0$ ,  $K \in \mathbb{N}$ ,  $C \subset \mathbb{R}^d$   
 $L_y$ : Lipschitz constant of  $\nabla \log p(y|x)$ .  
 $L$ : Lipschitz constant of  $\nabla \log q_\theta(x)$ .  
Output:  $\{X_k\}_{k=1}^K$

Set:  $k = 0$ ,  $\delta < (1/6)(L_y + \alpha L + 1/\lambda)^{-1}$

**while**  $k < K$  **do**

$Z_{k+1} \sim \mathcal{N}(0, I^d)$

$X_{k+1} = X_k + \delta \nabla \log p(y|X_k) + \delta \alpha \nabla \log q_\theta(X_k) +$

$\frac{\delta}{\lambda} (\Pi_C(X_k) - X_k) + \sqrt{2\delta} Z_{k+1}$

$k = k + 1$

**end while**

---

The parameter  $\alpha > 0$  controls how strongly the regularization of  $q_\theta$  is imposed. Also,  $\lambda$  controls the amount of the projection  $(\Pi_C - \text{Id})$  enforced. See Sec. III for theoretical analysis about the parameters and see Sec. IV for the guidance of selecting the parameters. One can efficiently compute  $\nabla \log q_\theta(x)$  using the automatic differentiation libraries in the standard deep learning frameworks (such as PyTorch).

**Remark:** In fact, Algorithm 1 only requires evaluating the log gradient  $\nabla \log q_\theta(x)$  and its Lipschitz constant. Our theoretical analysis in Sec. III depends on the properties of  $q_\theta(x)$  and holds even when  $q_\theta$  does not arise from a normalizing flow. This is essential since in our CT experiments in Sec. IV-C, we utilize *patchNR* [60], a normalizing flow-based regularizer which cannot generate  $x$  by (4) but is able to evaluate the log gradient  $\nabla \log q_\theta(x)$ .

It is imperative to understand why the projection  $(\Pi_C - \text{Id})$  is necessary for the convergence of NF-ULA. Let  $\iota_C^{(\lambda)}(x)$  be the  $\lambda$ -Moreau envelope [57] of the indicator function

$$\iota_C(x) = \begin{cases} 0, & x \in C, \\ +\infty, & x \notin C. \end{cases}$$

Then, we have that

$$\iota_C^{(\lambda)}(x) := \inf_{u \in \mathbb{R}^d} \left( \iota_C(u) + \frac{1}{2\lambda} \|x - u\|_2^2 \right) = \frac{1}{2\lambda} \|x - \Pi_C(x)\|_2^2,$$

$$\text{and } \nabla \iota_C^{(\lambda)}(x) = \frac{x - \text{Prox}_{\iota_C}(x)}{\lambda} = \frac{x - \Pi_C(x)}{\lambda},$$

where  $\Pi_C$  is the projection operator on the convex and compact (i.e., closed and bounded) set  $C \subset \mathbb{R}^d$ . Define  $p_\lambda(x|y)$  as

$$p_\lambda(x|y) = \frac{p(y|x)q_\theta^\alpha(x) \exp(-\iota_C^{(\lambda)}(x))}{\int_{\mathbb{R}^d} p(y|\tilde{x})q_\theta^\alpha(\tilde{x}) \exp(-\iota_C^{(\lambda)}(\tilde{x}))d\tilde{x}}, \quad (9)$$

where the exponent  $\alpha > 0$ . We show in Sec. III-B that  $p_\lambda(x|y)$  is well-defined and therefore  $(\Pi_C - \text{Id})$  is necessary for NF-ULA. Denote by  $\pi_{\lambda,y}$  (which we will write as  $\pi_\lambda$  for brevity) the probability measure whose density is  $p_\lambda(x|y)$  in (9), i.e.,

$$\frac{d\pi_\lambda}{d\pi_{\text{leb}}}(x) = p_\lambda(x|y), \quad (10)$$

where  $\pi_{\text{leb}}$  denotes the Lebesgue measure. Then, NF-ULA in Algorithm 1 is essentially equivalent to

$$X_{k+1} = X_k + \delta \nabla \log p_\lambda(X_k|y) + \sqrt{2\delta} Z_{k+1}. \quad (11)$$

We want to emphasize that in most of our experiments, NF-ULA is convergent while using a well-pre-trained normalizing flow, even without the projection term. This is presumably because the density  $q_\theta$  of a well-trained normalizing flow already satisfies the tail-decay condition [37] and most of the probability mass lies within  $C$ . For the cases where the normalizing flow is poorly trained, one should select a smaller  $C$ , without which the samples generated by NF-ULA will go far beyond our expected region (for imaging it is  $C_R = [0, 1]^d$ ).

### III. THEORETICAL ANALYSIS

Notations are given in Sec. III-A. We present some theoretical analysis for the Bayesian posterior  $p_\lambda(x|y)$  in Sec. III-B. Subsequently, we prove the convergence and non-asymptotic bias of NF-ULA in Sec. III-C.

#### A. Notations

Denote by  $\mathcal{B}(\mathbb{R}^d)$  the Borel  $\sigma$ -field of  $\mathbb{R}^d$ . For  $\mu$  a probability measure on  $(\mathbb{R}^d, \mathcal{B}(\mathbb{R}^d))$  and  $f$  a  $\mu$ -integrable function, denote by  $\mu(f)$  the integral of  $f$  w.r.t.  $\mu$ . For measurable  $f : \mathbb{R}^d \rightarrow \mathbb{R}$  and measurable  $V : \mathbb{R}^d \rightarrow [1, \infty)$ , the  $V$ -norm of  $f$  is defined as  $\|f\|_V = \sup_{\tilde{x} \in \mathbb{R}^d} |f(\tilde{x})|/V(\tilde{x})$ . Let  $\xi$  be a finite signed measure on  $(\mathbb{R}^d, \mathcal{B}(\mathbb{R}^d))$ . Then the  $V$ -total variation distance of  $\xi$  is defined as

$$\|\xi\|_V = \sup_{\|f\|_V \leq 1} \left| \int_{\mathbb{R}^d} f(\tilde{x}) d\xi(\tilde{x}) \right|. \quad (12)$$

Note that if  $V = 1$ , then  $\|\cdot\|_V$  is the total variation  $\|\cdot\|_{\text{TV}}$ . We denote  $\mathcal{P}(\mathbb{R}^d)$  the set of probability measures over  $(\mathbb{R}^d, \mathcal{B}(\mathbb{R}^d))$  and for any  $m \in \mathbb{N}$ ,  $\mathcal{P}_m(\mathbb{R}^d) = \{\nu \in \mathcal{P}(\mathbb{R}^d) : \int_{\mathbb{R}^d} \|\tilde{x}\|^m d\nu(\tilde{x}) < +\infty\}$ . Denote  $\mathbf{W}_1$  as the Wasserstein-1 metric.

Let  $b \in C(\mathbb{R}^d, \mathbb{R}^d)$  such that for any  $x \in \mathbb{R}^d$ , the following SDE admits a unique strong solution

$$d\mathbf{X}_t = b(\mathbf{X}_t) dt + \sqrt{2} d\mathbf{B}_t$$

$$\mathbf{X}_0 = x, \quad (13)$$

where  $(\mathbf{B}_t)_{t \geq 0}$  is a  $d$ -dimensional Brownian motion. For any  $x \in \mathbb{R}^d$  and  $A \in \mathcal{B}(\mathbb{R}^d)$ , equation (13) defines a Markov semi-group  $(P_t)_{t \geq 0}$  by  $P_t(x, A) = \mathbb{P}(\mathbf{X}_t \in A)$  where  $(\mathbf{X}_t)_{t \geq 0}$  is the solution of (13) with  $\mathbf{X}_0 = x$ . For any  $f \in C^2(\mathbb{R}^d, \mathbb{R})$ , define the generator  $\mathcal{A}$  of  $(P_t)_{t \geq 0}$  by  $\mathcal{A}f = \langle \nabla f, b(x) \rangle + \Delta f$ . We say that  $(P_t)_{t \geq 0}$  on  $\mathbb{R}^d \times \mathcal{B}(\mathbb{R}^d)$  with extended infinitesimal generator  $(\mathcal{A}, D(\mathcal{A}))$  (see e.g. [61] for the definition of  $(\mathcal{A}, D(\mathcal{A}))$ ) satisfies a continuous drift condition  $\mathbf{D}_c(W, \zeta, \beta)$  if there exist  $\zeta > 0, \beta \geq 0$  and a measurable function  $W : \mathbb{R}^d \rightarrow [1, +\infty)$  with  $W \in D(\mathcal{A})$  such that for all  $x \in \mathbb{R}^d$ ,

$$\mathcal{A}W(x) \leq -\zeta W(x) + \beta.$$

Similarly, we consider the Markov chain  $(X_k)_{k \in \mathbb{N}}$  given by the following recursion for any  $k \in \mathbb{N}$  and  $x \in \mathbb{R}^d$

$$X_{k+1} = X_k + \gamma b(X_k) + \sqrt{2\gamma} Z_k$$

$$X_0 = x,$$

with  $\gamma > 0$  and  $\{Z_k : k \in \mathbb{N}\}$  a family of i.i.d Gaussian random variables with zero mean and identity covariance matrix. We define its associated Markov kernel  $R_\gamma : \mathbb{R}^d \times \mathcal{B}(\mathbb{R}^d) \rightarrow [0, 1]$  as follows for any  $x \in \mathbb{R}^d$  and  $A \in \mathcal{B}(\mathbb{R}^d)$

$$R_\gamma(x, A) = \int_{\mathbb{R}^d} \mathbf{1}_A(x + \gamma b(x) + \sqrt{2\gamma}z) \exp[-\|z\|^2/2] dz.$$

We say that  $R_\gamma$  satisfies a discrete drift condition  $\mathbf{D}_d(W, \zeta_d, c)$  if there exist  $\zeta_d \in [0, 1), c \geq 0$  and a measurable function  $W : \mathbb{R}^d \rightarrow [1, +\infty)$  such that for all  $x \in \mathbb{R}^d$

$$R_\gamma W(x) \leq \zeta_d W(x) + c.$$

#### B. Well-posedness of the Bayesian solution

To start with, we give a lemma that will be used later.

**Lemma 1.** *For any convex and compact subset  $C$  of  $\mathbb{R}^d$  and for all  $k \in \mathbb{N}$ , it holds that*

$$\int_{\mathbb{R}^d} \|x\|^k \exp\left(-\frac{\|x - \Pi_C(x)\|_2^2}{2\lambda}\right) dx < +\infty.$$

*Proof.* See Appendix A. □

Lemma 1 implies that the integral of any polynomials multiplied by  $\exp(-\iota_C^{(\lambda)})$  is finite. To prove that  $p_\lambda(x|y)$  and  $\pi_\lambda$  are well-defined, besides Lemma 1, we need an assumption about the boundness of the prior and the likelihood:

**A 1.** *The distribution learned by NF is bounded, i.e.,  $\sup_{x \in \mathbb{R}^d} q_\theta(x) < +\infty$ . Moreover, for any  $y \in \mathbb{R}^m$ ,  $\sup_{x \in \mathbb{R}^d} p(y|x) < +\infty$  and  $p(y|\cdot) \in C^1(\mathbb{R}^d, (0, +\infty))$ .*

Since  $q_\theta(x)$  is a distribution induced by normalizing flow, in most cases  $\sup_{x \in \mathbb{R}^d} q_\theta(x)$  is bounded and A 1 is easily satisfied.

Using Lemma 1, we can then prove that the normalizing constant in the expression for  $p_\lambda(x|y)$  in (9) is finite:

**Corollary 1.** *Assume A 1. For any convex and compact set  $C$ , we have*

$$\int_{\mathbb{R}^d} p(y|x) q_\theta^\alpha(x) \exp\left(-\frac{\|x - \Pi_C(x)\|_2^2}{2\lambda}\right) dx < +\infty.$$

Hence,  $p_\lambda(x|y)$  in (9) is well-defined.

*Proof.* Letting  $k = 0$  in Lemma 1 and using A 1, we conclude the proof.  $\square$

**Remark:** Although  $\int_{\mathbb{R}^d} q_\theta(x) dx = 1$ ,  $\int_{\mathbb{R}^d} q_\theta^\alpha(x) dx$  may not be finite in rare cases. This depends on how heavy the tail of  $q_\theta(x)$  is. Corollary 1 shows that multiplying  $q_\theta^\alpha(x)$  with  $\exp(-\iota_C^{(\lambda)}(x))$  always leads to a finite integral, regardless the tail behavior of  $q_\theta(x)$ .

Now we can establish the well-posedness of  $\pi_\lambda$  in the following proposition, simply using SM5.3 in the supplementary materials [62] of [51].

**Proposition 1.** *Assume A 1 and that there exist continuous functions  $\Phi_1 : \mathbb{R}^d \rightarrow [0, +\infty)$  and  $\Phi_2 : \mathbb{R}^m \rightarrow [0, +\infty)$  such that for any  $x \in \mathbb{R}^d$  and  $y_1, y_2 \in \mathbb{R}^m$ , the following hold:*

$$\begin{aligned} & \left| \log(p(y_1|x)) - \log(p(y_2|x)) \right| \\ & \leq (\Phi_1(x) + \Phi_2(y_1) + \Phi_2(y_2)) \|y_1 - y_2\|, \text{ and} \\ & \int_{\mathbb{R}^d} (1 + \Phi_1(\tilde{x})) \exp\left[c_0 \Phi_1(\tilde{x}) - \iota_C^{(\lambda)}(\tilde{x})\right] d\tilde{x} < +\infty, \end{aligned}$$

for  $\forall c_0 > 0$ . Then,  $y \mapsto \pi_{\lambda,y}$  defined in (10) is locally Lipschitz w.r.t. the total-variation (TV) norm  $\|\cdot\|_{\text{TV}}$ , i.e., for any compact set  $K$  there exists  $M_K \geq 0$  such that for any  $y_1, y_2 \in K$ ,  $\|\pi_{\lambda,y_1} - \pi_{\lambda,y_2}\|_{\text{TV}} \leq M_K \|y_1 - y_2\|$ .

*Proof.* By A 1, we have that

$$\int_{\mathbb{R}^d} (1 + \Phi_1(\tilde{x})) \exp\left[c_0 \Phi_1(\tilde{x}) - \iota_C^{(\lambda)}(\tilde{x})\right] q_\theta^\alpha(\tilde{x}) d\tilde{x} < +\infty,$$

and we conclude the proof from Proposition SM5.3 in [62].  $\square$

### C. Convergence of NF-ULA

Most of the existing works on ULA for non-convex potentials [39], [47], [49]–[51] assume Lipschitz-continuity of the log gradient of the density. If  $\nabla \log p(x|y)$  is not Lipschitz, from [63], [64] it cannot generally be guaranteed that the SDE  $dX_t = \nabla \log p(X_t|y) dt + \sqrt{2} dB_t$  has a unique strong solution. This is why we must investigate the Lipschitz condition of  $\nabla \log p_\lambda(x|y)$  before studying the convergence of NF-ULA.

Firstly, we make a mild assumption about the Lipschitz-continuity of  $\nabla \log(p(y|\cdot))$ :

**A 2.** *There exists  $L_y > 0$  such that  $\nabla \log(p(y|\cdot))$  is  $L_y$ -Lipschitz continuous.*

Note that A 2 is an easily satisfied condition in imaging inverse problems. One example is the Gaussian likelihood where  $p(y|x) \propto \exp(-\|y - Ax\|_2^2 / (2\sigma^2))$ . Under A 2, we

can show that the Lipschitz continuity of  $\nabla \log p_\lambda(x|y)$  is equivalent to that of  $\nabla \log q_\theta(x)$ :

**Lemma 2.** *Assume A 2. Then,  $\nabla \log p_\lambda(x|y)$  is Lipschitz continuous if and only if  $\nabla \log q_\theta(x)$  is Lipschitz continuous.*

*Proof.* See Appendix B.  $\square$

For convenience, we explicitly define the Lipschitz condition on the log gradient of  $q_\theta(x)$  in the following assumption:

**A 3.** *There exist  $L \geq 0$  such that for any  $x_1, x_2 \in \mathbb{R}^d$ ,*

$$\|\nabla \log q_\theta(x_1) - \nabla \log q_\theta(x_2)\| \leq L \|x_1 - x_2\|.$$

It is therefore natural to ask how to enforce A 3 on  $q_\theta(x)$  during training or by the network architecture. Although there have been some studies about the Lipschitz continuity of the invertible transform  $T_\theta$  [55], [65], [66], to the best of our knowledge, there is no study about the Lipschitz continuity of  $\nabla \log q_\theta(x)$  until now.

While the equivalent conditions on  $T_\theta$  for A 3 remain unknown, it should be noted that the sufficient condition on  $T_\theta$  can be obtained easily. For instance, when  $T_\theta$  is a linear transform mapping a Gaussian distribution  $q_z(z)$  to another Gaussian distribution  $q_\theta(x)$ , assumption A 3 holds. However, this may not be true if  $T_\theta$  is nonlinear.

To give a sufficient condition on  $T_\theta$  for A 3, we refer to some studies of tails of normalizing flows [67]. Theorem 4 in [67] shows that affine coupling layer-based flows (NICE [68], Real-NVP [54], MAF [69], IAF [70], Glow [56]) can only map the base normal distribution  $q_z(z)$  to a light-tailed distribution  $q_\theta(x)$ . To be more specific, denote  $G(x) = T^{-1}(x)$ , where  $G(x)$  is a triangular mapping and the Jacobian  $J_G(x)$  is a triangular matrix function. From [67], generally one can assume that the affine coupling layer-based flows  $G_j(x_j, x_{<j}) = \varphi_j(x_{<j})x_j + \eta_j(x_{<j})$ , where  $G_j$  is the  $j$ -th element of the vector  $G(x)$  and  $x_{<j}$  indicate  $x_1, \dots, x_{j-1}$ . Note that the light tail of  $q_\theta(x)$  does not necessarily imply the Lipschitz of  $\nabla \log q_\theta(x)$ , but the condition they assume is heuristic: if  $\varphi_j$  is bounded above and  $\eta_j$  is Lipschitz, then  $q_\theta(x)$  is light-tailed. In Glow [56] these conditions on  $\varphi$  and  $\eta$  are satisfied and even stricter. Therefore we are able to prove the Lipschitz of  $\nabla \log q_\theta(x)$  in the proposition below, by enforcing a stricter condition on  $\varphi$  and  $\eta$ :

**Proposition 2.** *Assume that  $q_z(z)$  is standard normal distribution. Denote  $G(x) = T^{-1}(x)$  and assume the affine coupling layer  $G_j(x_j, x_{<j}) = \varphi_j(x_{<j})x_j + \eta_j(x_{<j})$ ,  $j = 1, \dots, d$ . If  $\varphi_j$  is a constant function,  $\eta_j$  is Lipschitz,  $\forall i < j$ ,  $\frac{\partial \eta_j}{\partial x_i}$  is well-defined almost everywhere and piecewise constant on  $\mathbb{R}$ , then  $\nabla \log q_\theta(x)$  is Lipschitz continuous on  $\mathbb{R}^d$ .*

*Proof.* See Appendix C.  $\square$

The conditions on  $\varphi, \eta$  in Proposition 2 are exactly satisfied in Glow [56] of additive coupling layers. Conditions on  $\eta$  are satisfied because it is a 5-layer sequential net by ReLU and Conv2d layers

$$\eta(x) = \text{Conv2d}(\text{Relu}(\text{Conv2d}(\text{Relu}(\text{Conv2d}(x))))),$$

meanwhile  $\varphi = 1$  is used in additive coupling layer. Note that in Glow there is another option using affine coupling layer where  $\varphi$  is sigmoid function. This leads to a more powerful network and can generate better human face images [56] but  $\nabla \log q_\theta(x)$  is not Lipschitz. This matches to the experiments in Sec. IV-A. The conditions on  $\varphi$  and  $\eta$  might be relaxed if  $q_z(z)$  is not Gaussian, but this requires re-training the net since most of the popular normalizing flows has standard Gaussian base distribution. Hence we leave these possible studies on the Lipschitz-continuity of  $\nabla \log q_\theta(x)$  for future work.

In what follows, we introduce the associated stochastic kernel  $R_\delta : \mathbb{R}^d \times \mathcal{B}(\mathbb{R}^d) \rightarrow [0, 1]$  of the NF-ULA (11) and the drift  $b_\lambda(x)$ :

$$\begin{aligned} R_\delta(x, A) &= (2\pi)^{-d/2} \int_{\mathbb{R}^d} \mathbf{1}_A \left( x + \delta b_\lambda(x) + \sqrt{2\delta}z \right) \exp[-\|z\|^2/2] dz, \\ b_\lambda(x) &= \nabla \log p_\lambda(x|y) \\ &= \nabla \log p(y|x) + \alpha \nabla \log q_\theta(x) + \frac{\Pi_C(x) - x}{\lambda}, \end{aligned} \quad (14)$$

where  $x \in \mathbb{R}^d$  and  $A \in \mathcal{B}(\mathbb{R}^d)$ . In NF-ULA (11) the variable  $Z_{k+1}$  is i.i.d. drawn from standard Gaussian and thus in  $R_\delta$  there is a  $z$  with density  $(2\pi)^{-d/2} \exp[-\|z\|^2/2]$ . Given  $X_k$  in NF-ULA (11),  $R_\delta(X_k, \cdot)$  is actually a probability measure which defines the same distribution of  $X_{k+1}$ . To prove the convergence of NF-ULA, we need the last assumption:

**A 4.** *There exists  $m \in \mathbb{R}$  such that for any  $x_1, x_2 \in \mathbb{R}^d$  we have*

$$\begin{aligned} \langle \nabla \log p(y|x_2) - \nabla \log p(y|x_1), x_2 - x_1 \rangle \\ \leq -m \|x_2 - x_1\|_2^2. \end{aligned}$$

This condition is called the contractivity condition of  $\nabla \log p(y|x)$  and is later used to prove the contractivity at infinity condition of  $b_\lambda(x)$ . Note that the influence of the drift's contractivity condition has been studied in ULA on non-convex potentials [47]–[49].

If A 4 is satisfied with  $m > 0$ , then  $x \mapsto -\log p(y|x)$  is actually  $m$  strongly-convex. Assume A 2, then A 4 holds for  $m = -L_y$ . However, we are interested to find  $m > -L_y$  while assuming A 2, since we will see later that a larger  $m$  is beneficial to the convergence of NF-ULA.

With all the previous four assumptions holding, we can now prove that NF-ULA (Algorithm 1) is convergent, or more precisely, the stochastic kernel  $R_\delta$  admits an invariant distribution  $\pi_{\delta, \lambda}(x)$ . We follow the proof in SM6.2 from [62]. The first thing to prove is that  $R_\delta$  defines a contractive mapping.

**Theorem 1.** *Assume A 1, A 2, A 3, and A 4. Assume  $V = 1 + \|x\|^2$ . Let  $\lambda, \alpha, C, L_y, L$  be the ones in NF-ULA (Algorithm 1). Let  $m$  be the parameter in A 4. Let  $\lambda > 0$ , such that  $2\lambda(L_y + \alpha L - \min(m, 0)) \leq 1$  and let  $\bar{\delta} = (1/6)(L_y + \alpha L + 1/\lambda)^{-1}$ . Then for any convex and compact  $C$  with  $0 \in C$ , there exist  $A_1 \geq 0$  and  $\rho_1 \in [0, 1)$*

*such that for any  $\delta \in (0, \bar{\delta}]$ ,  $x_1, x_2 \in \mathbb{R}^d$ , and  $k \in \mathbb{N}$  we have*

$$\begin{aligned} \|\delta_{x_1} R_\delta^k - \delta_{x_2} R_\delta^k\|_V &\leq A_1 \rho_1^{k\delta} (V^2(x_1) + V^2(x_2)), \\ \mathbf{W}_1(\delta_{x_1} R_\delta^k, \delta_{x_2} R_\delta^k) &\leq A_1 \rho_1^{k\delta} \|x_1 - x_2\|_2. \end{aligned}$$

*Proof.* See Appendix D. □

In the above theorem the Dirac measures  $\delta_{x_1}, \delta_{x_2}$  can be extended to any measures  $\nu_1, \nu_2 \in \mathcal{P}_1(\mathbb{R}^d)$ :

$$\begin{aligned} \|\nu_1 R_\delta^k - \nu_2 R_\delta^k\|_V &\leq A_1 \rho_1^{k\delta} \left( \int_{\mathbb{R}^d} V^2(\tilde{x}) d\nu_1(\tilde{x}) + \int_{\mathbb{R}^d} V^2(\tilde{x}) d\nu_2(\tilde{x}) \right), \\ \mathbf{W}_1(\nu_1 R_\delta^k, \nu_2 R_\delta^k) &\leq A_1 \rho_1^{k\delta} \left( \int_{\mathbb{R}^d} \|\tilde{x}\| d\nu_1(\tilde{x}) + \int_{\mathbb{R}^d} \|\tilde{x}\| d\nu_2(\tilde{x}) \right). \end{aligned} \quad (15)$$

From Theorem 6.18 in [71],  $(\mathcal{P}_1(\mathbb{R}^d), \mathbf{W}_1)$  is a complete metric space. For any measure  $\nu \in \mathcal{P}_1(\mathbb{R}^d)$ , define  $f : \mathcal{P}_1(\mathbb{R}^d) \rightarrow \mathcal{P}_1(\mathbb{R}^d)$  as  $f(\nu) = \nu R_{\varepsilon, \delta}$ . Then for any  $\delta \in (0, \bar{\delta}]$ , there exists large enough  $m \in \mathbb{N}^*$  such that  $f^m$  is a contractive mapping. Therefore we can apply the Picard fixed point theorem and we obtain that  $R_\delta$  admits an invariant probability measure  $\pi_{\delta, \lambda} \in \mathcal{P}_1(\mathbb{R}^d)$ . Since  $\pi_{\delta, \lambda}$  is subject to bias comparing with the solution of the SDE  $dX_t = b_\lambda(X_t)dt + \sqrt{2\delta} dB_t$ , we follow the proof in SM6.3 from [62] and give a nonasymptotic bias analysis:

**Theorem 2.** *Assume A 1, A 2, A 3, A 4. Assume  $V = 1 + \|x\|^2$ . Let  $\lambda, \alpha, C, L_y, L$  be the ones in NF-ULA (Algorithm 1). Let  $m$  be the parameter in A 4. Let  $\lambda > 0$  such that  $2\lambda(L_y + \alpha L - \min(m, 0)) \leq 1$  and let  $\bar{\delta} = (1/6)(L_y + \alpha L + 1/\lambda)^{-1}$ . Then for any  $\delta \in (0, \bar{\delta}]$  and  $C$  convex and compact,  $R_\delta$  admits an invariant probability measure  $\pi_{\delta, \lambda}$ . In addition, there exists  $B_1, B_2 \geq 0$ ,  $\tilde{\rho}_1 \in [0, 1)$  such that for any  $\delta \in (0, \bar{\delta}]$ ,  $k \in \mathbb{N}^*$ ,*

$$\|\delta_x R_\delta^k - \pi_\lambda\|_V \leq B_1 \tilde{\rho}_1^{k\delta} V^2(x) + B_2 V(x) \sqrt{\delta^2 k}.$$

*Proof.* See Appendix E. □

**Remark:** Note that there is a trade-off of selecting the step-size  $\delta$ . In order to achieve a small bias, one needs to set a large time interval  $t = k\delta$ , keep  $t$  fixed and use a small step size  $\delta$ . However, larger  $k$  means drawing more samples and longer computation time. In practice, the burn-in period is incorporated in  $t$ , in which the Markov Chain is dramatically exploring the state space.

## IV. EXPERIMENTS IN BAYESIAN IMAGING

We perform NF-ULA and PnP-ULA on three Bayesian inverse problems: image motion deblurring, image inpainting and limited-angle computed tomography (CT) reconstruction. We compare with PnP-ULA because both NF-ULA and PnP-ULA are Langevin algorithms with learning-based non-convex regularizers.

**Guidance for choosing  $\alpha$ :** For both NF-ULA and PnP-ULA on different problems, we fine tune  $\alpha$  such that the PSNR of



Fig. 1. Images generated by unconditional sampling  $x = T_\theta(z)$ ,  $z \sim 0.7\mathcal{N}(0, I^d)$ , using Glow (additive coupling layers) trained on FFHQ. Column 1: Glow trained for 5 epochs. Column 2: Glow trained for 20 epochs. Column 3: Glow trained for 100 epochs.

the sample mean is as good as possible. While in most cases  $\alpha \in (0, 5]$  works well, for NF-ULA it is also related to the architecture of the normalizing flow. In CT reconstruction, we use the pre-trained patchNR from the code provided in [60] and choose  $\alpha = 5000$ , while in the original code they set  $\alpha = 700$ .

**Guidance for choosing  $C$  and  $\lambda$ :** From [51],  $(\text{Id} - \Pi_C)$  is introduced to PnP-ULA to make sure the posterior satisfies the tail decay condition. Therefore for those posterior distributions which are originally less tail-decaying, a smaller  $C$  is recommended. From our experiments, NF-ULA is numerically stable using the normalizing flow trained for more than 20 epochs, even with a large  $C$ . For the normalizing flow which is not well trained (less than 5 epochs), it is recommended that  $C$  should be the same as the range  $C_R$  of the dataset. In the imaging problems we have that  $C_R = [0, 1]^d$ . See Table I for details. For well trained normalizing flows in NF-ULA and denoiser in PnP-ULA, we set  $C = [-100, 100]^d$ . Actually all the samples generated in Table II, III, IV, V never escape  $[-0.2, 1.2]^d$ , indicating that the projection  $\Pi_C(x)$  is never activated. We keep  $\lambda = 5$ , even though different  $\lambda$  makes no difference in most of our experiments.

**Guidance for choosing  $\delta$ :** From Theorem 1 and Theorem 2, any  $\delta < (1/6)(L_y + \alpha L + 1/\lambda)^{-1}$  should work. However, in practice it is not easy to know the Lipschitz constant  $L$  of  $\nabla \log q_\theta(x)$ . Moreover, small  $L$  implies that  $(L_y + \alpha L + 1/\lambda)$  is dominated by  $L_y$ , which can be easily computed depending on the considered forward operator. Therefore in most of our experiments  $\delta$  is chosen to be smaller than  $(1/10)L_y^{-1}$ , to make sure the convergence of different algorithms.

**Computation implementations:** We implement all the experiments under Python and PyTorch library. Codes will be available upon acceptance of this work. They are run on Intel(R) Xeon(R) Platinum 8358P CPU with four Nvidia Tesla A100 GPU.

### A. Deblurring

We start with a non-blind motion deblurring problem on human face images. We define the forward operator  $A$  by

convolving the image  $x$  with a  $9 \times 9$  motion blurring kernel, with all the elements in the 5-th row being  $1/9$  and the other rows being 0. Both  $x, y \in \mathbb{R}^d = \mathbb{R}^{3 \times 128 \times 128}$  and the linear operator  $A : \mathbb{R}^{3 \times 128 \times 128} \rightarrow \mathbb{R}^{3 \times 128 \times 128}$ . To formalize the forward model, we add a Gaussian noise  $n \sim \sigma\mathcal{N}(0, I^d)$ :

$$y = Ax + n, \quad p(y|x) = \frac{1}{(2\pi\sigma^2)^{d/2}} \exp\left(-\frac{\|y - Ax\|^2}{2\sigma^2}\right).$$

**Network training:** To realize NF-ULA, we train the well-known flow-based model, Glow [56], on the human face dataset FFHQ [72] without the first 20 images, which are 69980 images in total. All the images are 3-channel images normalized into  $C_R = [0, 1]^{3 \times 128 \times 128}$ . We train Glow by the PyTorch code<sup>1</sup>. The architecture of Glow has 5 blocks with 32 flows in each block.

For PnP-ULA, [51] use the real spectral normalization DnCNN (realSN-DnCNN), the Lipschitz continuous denoiser proposed in [52]. In order to see the behavior of the denoiser without Lipschitz condition, we train both the standard DnCNN [73] and realSN-DnCNN [52] on the image patches of a 980-image subset of FFHQ. To train the denoiser, we follow the instructions in [51] to add Gaussian noise with the variance  $\varepsilon = (5/255)^2$  on the training data batches. To train the standard DnCNN, we directly use the code in the Image Restoration Toolbox<sup>2</sup>. We keep the default parameter settings to train the 17-layers DnCNN on image patches with size 40. For realSN-DnCNN, the original code<sup>3</sup> in [52] only support training on grayscale images, therefore we modified the code to make it applicable to 3-channel images. We also set up the network layers as 17 and preprocess the data to patches with size 40, while setting the Lipschitz parameter, an additional parameter in realSN-DnCNN, to 1. It should be clear that even DnCNN and realSN-DnCNN are trained on such a small set, they can still obtain a PSNR of more than 40 on the validation set. In fact, the original code in [52] defaultly train the denoiser on a dataset of merely 400 images and continuing

<sup>1</sup><https://github.com/rosinality/glow-pytorch>

<sup>2</sup><https://github.com/cszn/KAIR>

<sup>3</sup>[https://github.com/uclaopt/Provable\\_Plug\\_and\\_Play/](https://github.com/uclaopt/Provable_Plug_and_Play/)

TABLE I  
BEHAVIORS OF NF-ULA BY DIFFERENT GLOW.

Deblurring	network	coupling layers	epochs	parameters	C	PSNR
face1						
NF-ULA	Glow	affine	100	$\alpha = 1.5$	$[0, 1]^d$	divergent
NF-ULA	Glow	additive	5	$\alpha = 1.5$	$[-100, 100]^d$	divergent
NF-ULA	Glow	additive	5	$\alpha = 1.5$	$[0, 1]^d$	26.58
NF-ULA	Glow	additive	20	$\alpha = 1.5$	$[-100, 100]^d$	29.84
NF-ULA	Glow	additive	100	$\alpha = 1.5$	$[-100, 100]^d$	30.42

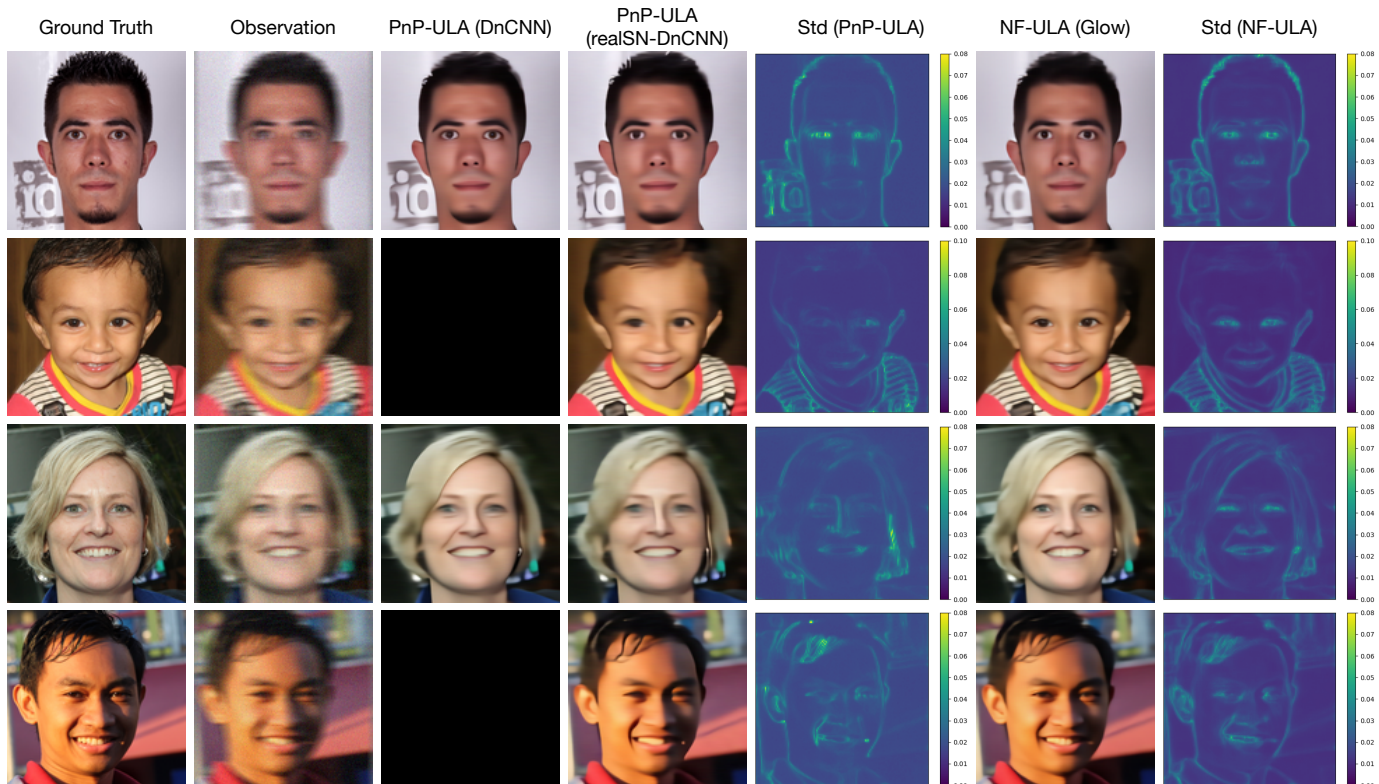


Fig. 2. Deblurring by PnP-ULA and NF-ULA. Column 1: Original images. Column 2: Blurred images (observations). Column 3: Posterior mean by PnP-ULA (DnCNN). Column 4: Posterior mean by PnP-ULA (realSN-DnCNN). Column 5: Standard deviation (2-th channel) of the samples by PnP-ULA (realSN-DnCNN). Column 6: Posterior mean by NF-ULA (Glow). Column 7: Standard deviation (2-th channel) of NF-ULA (Glow). PSNR of the samples mean are provided in Table II.

to increase the size of dataset does not considerably implies a higher PSNR on the validation set.

The Glow we used has 100870544 parameters in total, while DnCNN has 559363 parameters and realSN-DnCNN has 558336 parameters. To train 100 epochs, Glow spent up to 100 hours, while DnCNN and realSN-DnCNN spent less than 5 hours.

**ULA parameters settings:** We set the standard deviation of the Gaussian noise as  $\sigma = 0.02$ . To ensure that every algorithm is numerically stable, we select the step size  $\delta = 5 \times 10^{-5}$ . For Glow, DnCNN and realSN-DnCNN,  $\alpha = 1.5$  implies the highest PSNR. We initialize  $X_0 = y$ , the noisy blurred observation for both NF-ULA and PnP-ULA.

**Behaviors of the algorithms:** To explore the state space thoroughly, all the experiments have burn-in iterations less than 5000. Since  $X_0$  is initialized as the observation  $y$ , the PSNR of  $X_n$  starts from around 22.78, keeps going up and is finally balanced. Only after the burn-in time, we calculate the

posterior mean by obtaining 10000 samples and compute the PSNR of the samples mean. To draw 10000 samples, NF-ULA spend around 3100 seconds and PnP-ULA spend 30 seconds. This is mainly because of the large network Glow uses - the Glow we use has more than 100 times parameters than realSN-DnCNN. In fact, we found out that computing and forwarding the auto-gradient function of  $q_\theta(x)$  is spending 10% longer time than forwarding  $q_\theta(x)$  itself. Even though, we believe that NF-ULA has great potentials to leverage smaller and more advanced normalizing flow induced prior to reduce the computational time.

Firstly, to see whether the Lipschitz condition of  $\nabla \log q_\theta(x)$  is true for different kinds of coupling layers, we train two different Glow respectively with affine coupling layers and additive coupling layers, all for 100 epochs. Also, to verify our hypothesis that better training of the normalizing flow will imply better samples from NF-ULA, we respectively trained Glow (additive coupling layers) for 5, 20 and 100 epochs.

TABLE II  
DEBLURRING: COMPARISON OF THE ULA WITH DIFFERENT PRIORS.

Deblurring	network	epochs	parameters	$C$	PSNR
face1					
NF-ULA	Glow	100	$\alpha = 1.5$	$[-100, 100]^d$	30.42
PnP-ULA	DnCNN	100	$\alpha = 1.5$	$[-100, 100]^d$	30.40
PnP-ULA	realSN-DnCNN	100	$\alpha = 1.5$	$[-100, 100]^d$	30.42
face2					
NF-ULA	Glow	100	$\alpha = 1.5$	$[-100, 100]^d$	29.81
PnP-ULA	DnCNN	100	$\alpha = 1.5$	$[-100, 100]^d$	divergent
PnP-ULA	realSN-DnCNN	100	$\alpha = 1.5$	$[-100, 100]^d$	29.38
face3					
NF-ULA	Glow	100	$\alpha = 1.5$	$[-100, 100]^d$	30.70
PnP-ULA	DnCNN	100	$\alpha = 1.5$	$[-100, 100]^d$	29.61
PnP-ULA	realSN-DnCNN	100	$\alpha = 1.5$	$[-100, 100]^d$	29.39
face4					
NF-ULA	Glow	100	$\alpha = 1.5$	$[-100, 100]^d$	30.34
PnP-ULA	DnCNN	100	$\alpha = 1.5$	$[-100, 100]^d$	divergent
PnP-ULA	realSN-DnCNN	100	$\alpha = 1.5$	$[-100, 100]^d$	29.71

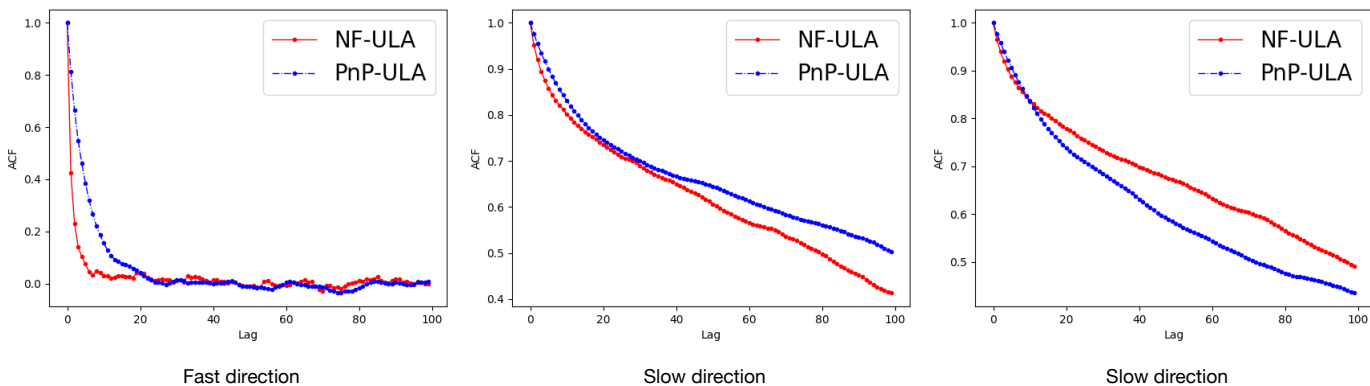


Fig. 3. The autocorrelation function (ACF) of the samples (deblurring).

Fig 1 shows the images generated by different Glow. Then we perform NF-ULA with these Glow, draw samples and calculate the posterior mean. The PSNR is given in Table I. When using affine coupling layers, NF-ULA fails to converge because  $\nabla \log q_\theta(x)$  is roughly not Lipschitz continuous, which matches Proposition 2. For Glow with additive coupling layers and well trained Glow (more than 20 epochs), NF-ULA works well and the generated samples do not diverge, even  $C = [-100, 100]^d$  is much larger than  $C_R$ . This suggests that the well trained prior  $q_\theta(x)$  already satisfies the tail decay conditions, without imposing the projection  $\text{Id} - \Pi_C$ . However, it is still essential for the theoretical study. For poorly trained Glow (less than 5 epochs) and large  $C$ , NF-ULA does not work well - most of the samples go far beyond  $C_R$  and the PSNR of them are below 10. If  $C$  is set to be a much smaller set, e.g.,  $C = C_R$ , then the PSNR can be up to 26, but still much lower than the well trained case.

Intuitively,  $q_\theta(x)$  is more diffusive when Glow is trained for only a few epochs. After training for some epochs, the normalizing flows is more suitable to serve as an image prior, the density  $q_\theta(x)$  is more concentrated and hence the tail decay condition of  $p(x|y)$  is already satisfied, even without the projection  $\Pi_C(x)$ .

Secondly, to see the ULA with different priors - PnP prior and normalizing flow induced prior, we run NF-ULA by Glow,

PnP-ULA by DnCNN and PnP-ULA by realSN-DnCNN on 4 human face images selected from the first 20 images of FFHQ [72]. In the following experiments, we use Glow with additive coupling layers. Glow, DnCNN and realSN-DnCNN are trained for 100 epochs for fairly comparison. Details are given in Fig 2 and Table II. From Table II, NF-ULA with Glow generates samples with the highest PSNR. We also present the standard deviation of the samples on the same channel in Fig 2. NF-ULA has richer details for posterior mean and more variations for standard deviation, particularly on the eyes, mouths and hairs. This is probably due to the suitable prior learned by the generative model. It is worth noting that PnP-ULA with DnCNN shows great performance on face1 and face3, but is divergent on face2 and face4. Meanwhile, PnP-ULA with realSN-DnCNN converges on all images.

One common method to know the convergence speeds of a Markov chain is to calculate the  $d$ -dimensional autocorrelation function (ACF) of it. Faster decreasing ACF generally implies faster convergence of the Markov chain. Notably the calculation of ACF is not easy in high dimensional problems. To characterize the Markov chain generated by NF-ULA (Glow) and PnP-ULA (realSN-DnCNN), we randomly select 100 dimensions from the total  $3 \times 128 \times 128$  dimensions and calculate the ACF on those dimensions. It should be noted that the ACF have different decreasing speeds among different

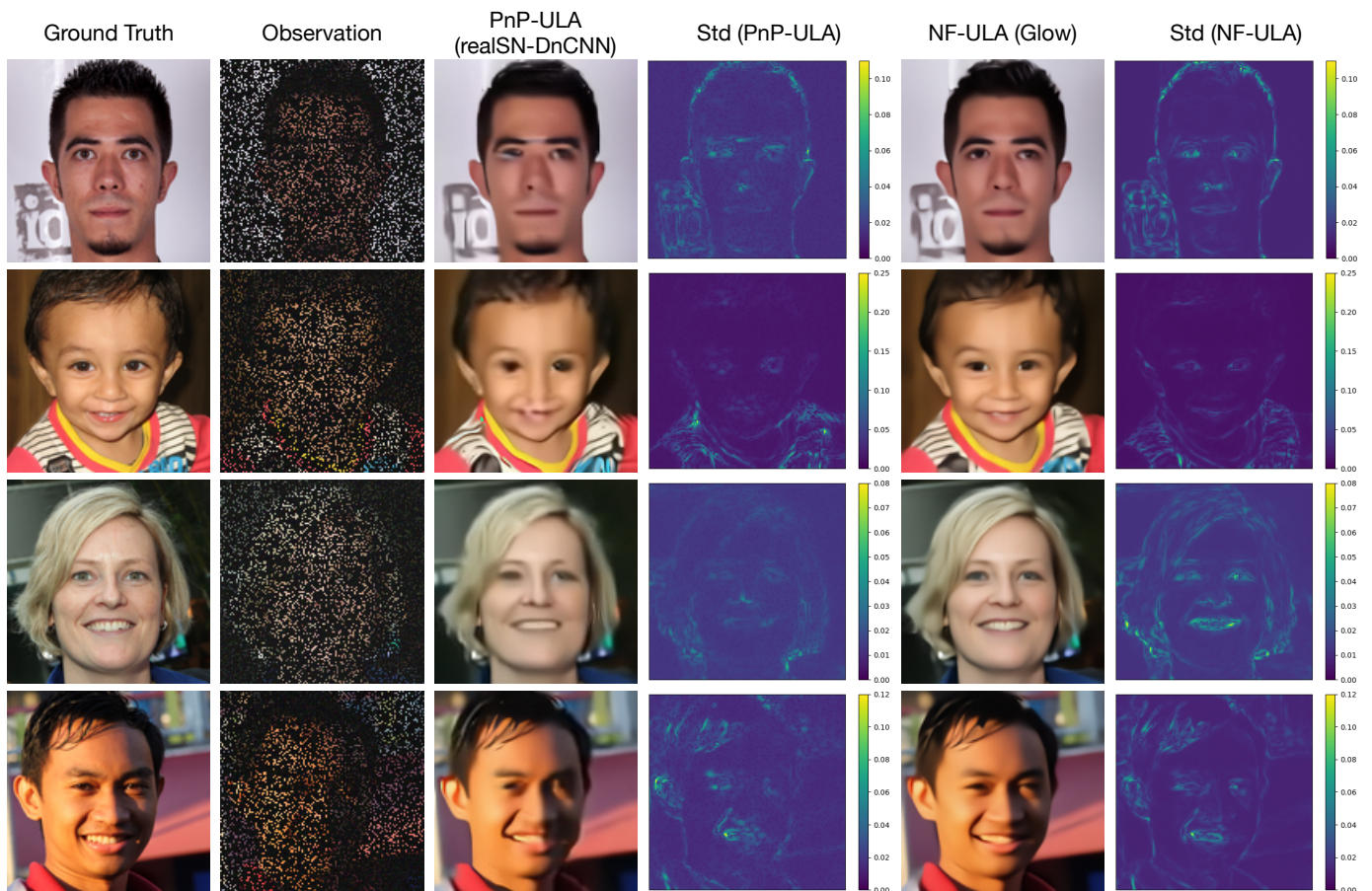


Fig. 4. Inpainting by PnP-ULA and NF-ULA. Column 1: Original images. Column 2: Images with 80% missing pixels. (observations). Column 3: Posterior mean by PnP-ULA (realSN-DnCNN). Column 4: Standard deviation (2-th channel) of samples by PnP-ULA (realSN-DnCNN). Column 5: Posterior mean by NF-ULA (Glow). Column 6: Standard deviation (2-th channel) of samples by NF-ULA (Glow). PSNR of the samples mean are provided in Table III.

directions, therefore it is time-consuming to analyze the ACF of all the image dimensions and calculate the fastest and slowest decreasing direction. In Fig 3, we provide 1 ACF of fast direction and 2 of slow direction. Among those fast directions, the ACF of PnP-ULA is decreasing from 1 to 0 within 20 lags, while for NF-ULA it is even faster and within 10 lags. For slow directions, both NF-ULA and PnP-ULA hold a non-zero ACF until more than 100 lags, and it is hard to say which method is decreasing faster.

### B. Inpainting

In this section we present the experimental results of image inpainting. We still focus on the problems on human face images and directly use the Glow and realSN-DnCNN trained in Sec. IV-A. Different from deblurring, we change the blurring operator  $A$  to the operator masking on  $x$  with 80% pixels in  $x$  missed. We choose different  $\alpha$  to ensure both NF-ULA and PnP-ULA have the best performance:  $\alpha = 2.0$  works fine for NF-ULA, while for PnP-ULA  $\alpha = 2.5$  is better. We maintain the other settings such as the noise standard deviation  $\sigma = 0.02$ , the dimension of image and observation  $x, y \in \mathbb{R}^d = \mathbb{R}^{3 \times 128 \times 128}$ , the step-size of both algorithms  $\delta = 5 \times 10^{-5}$ , the convex set  $C = [-100, 100]^d$  and the initialization  $X_0 = y$ .

**Behaviors of the algorithms:** Compared to deblurring, both NF-ULA and PnP-ULA have much longer burn-in time. We initialize  $X_0$  to be observation  $y$ , whose PSNR is only 5.46. NF-ULA has a burn-in iteration of 10000 until the PSNR of  $X_n$  grows more than 25 and becomes stable, while PnP-ULA takes a 80000-iteration burn-in time. The reason might be that Glow’s powerful prior information accelerates the burn-in process, particularly on the pixels missing in the observation. After the burn-in time, we draw 10000 samples and compute the PSNR of the samples mean. Drawing 10000 samples spend nearly the same time as in the deblurring experiment.

The samples mean and the standard deviation are given in Fig 4. Compared to PnP-ULA, NF-ULA recovers more areas of the faces and shows reasonable uncertainties on eyes, hairs, noses and teeth. From Table III, NF-ULA achieves higher PSNR than PnP-ULA. For both NF-ULA and PnP-ULA, the PSNR of the posterior mean is lower than deblurring - forward operator of masking 80% pixels is not invertible and the observation  $y$  in inpainting is less helpful to the reconstruction, which means that in the Bayesian perspective the samples are more relying on the prior than the likelihood.

To calculate the ACF in this inpainting results, we use the same strategy as in deblurring: calculating the ACF on 100 randomly selected dimensions of  $\{X_i\}_{i=1}^{10000}$ . We give the

TABLE III  
INPAINTING: COMPARISON OF THE ULA WITH DIFFERENT PRIORS.

Inpainting	network	epochs	parameters	$C$	PSNR
face1					
NF-ULA	Glow	100	$\alpha = 2$	$[-100, 100]^d$	28.02
PnP-ULA	realSN-DnCNN	100	$\alpha = 2.5$	$[-100, 100]^d$	25.80
face2					
NF-ULA	Glow	100	$\alpha = 2$	$[-100, 100]^d$	25.04
PnP-ULA	realSN-DnCNN	100	$\alpha = 2.5$	$[-100, 100]^d$	22.17
face3					
NF-ULA	Glow	100	$\alpha = 2$	$[-100, 100]^d$	29.18
PnP-ULA	realSN-DnCNN	100	$\alpha = 2.5$	$[-100, 100]^d$	27.40
face4					
NF-ULA	Glow	100	$\alpha = 2$	$[-100, 100]^d$	28.26
PnP-ULA	realSN-DnCNN	100	$\alpha = 2.5$	$[-100, 100]^d$	26.23

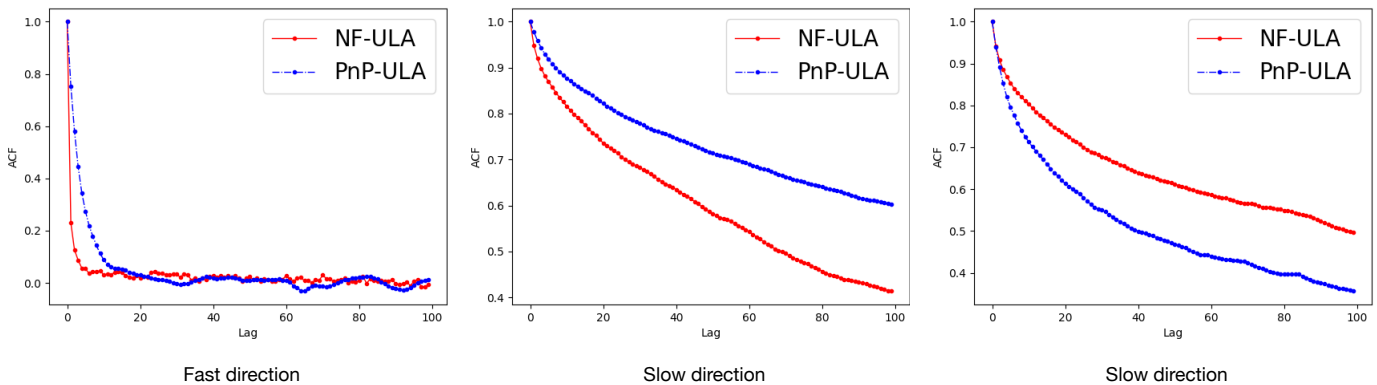


Fig. 5. The autocorrelation function (ACF) of the samples (inpainting).

TABLE IV  
CT RECONSTRUCTION OF GAUSSIAN NOISE, LIMITED ANGLES.

CT	network	parameters	$C$	PSNR
figure1				
NF-ULA	PatchNR	$\alpha = 5000$	$[-100, 100]^d$	29.65
PnP-ULA	realSN-DnCNN	$\alpha = 3$	$[-100, 100]^d$	26.60
figure2				
NF-ULA	PatchNR	$\alpha = 5000$	$[-100, 100]^d$	34.50
PnP-ULA	realSN-DnCNN	$\alpha = 3$	$[-100, 100]^d$	28.30
figure3				
NF-ULA	PatchNR	$\alpha = 5000$	$[-100, 100]^d$	31.66
PnP-ULA	realSN-DnCNN	$\alpha = 3$	$[-100, 100]^d$	30.08
figure4				
NF-ULA	PatchNR	$\alpha = 5000$	$[-100, 100]^d$	30.09
PnP-ULA	realSN-DnCNN	$\alpha = 3$	$[-100, 100]^d$	26.83

ACF including one fast direction and two slow directions in Fig 5. Similar to Fig 3, among those fast decreasing directions, the ACF of NF-ULA is slightly faster than PnP-ULA and they both decrease from 1 to 0 within 20 lags. For slow directions, we still cannot conclude which method is decreasing faster.

### C. CT Reconstruction

In this section, we consider a more challenging problem: CT reconstruction with limited angles. We use the library torch\_radon [74] to model the forward operator  $A$  by fan beam geometry. Instead of considering angles within  $[0, 2\pi]$ , we only have access to a subset  $[0.1 * \pi, 0.9 * \pi]$  of angles. We set the

number of detectors to 144, and test the algorithms for both Gaussian noise and Poisson noise (in Appendix F):

$$y = A(x) + n, \quad (16)$$

where  $+n$  is denoted as adding a Gaussian or Poisson noise. The image space is  $x \in \mathbb{R}^{362 \times 362}$  and the sinogram is  $y \in \mathbb{R}^{144 \times 512}$ . To estimate the norm of  $A$ , we found that approximately  $A(x) \in [0, 100]^{144 \times 512}$  for  $x \in [0, 1]^{362 \times 362}$ .

**Network settings:** To the best of our knowledge, the features and textures of medical images are more difficult to be learned than natural images. Hence normalizing flows do not have comparable performance in generating semantically meaningful images on medical imaging, comparing with natural images. Therefore we use a normalizing flow based prior, patchNR [60], to test NF-ULA on CT reconstruction. PatchNR is a powerful regularizer involves GlowCoupling layers learned on small patches of very few images, which has showed promising results on CT reconstruction trained on just six images [60]. PatchNR uses the FrEIA package [75] and takes advantages of a much smaller network than Glow. It should be noted that extracting the patches from an image is not a bijection, therefore patchNR is actually learning the prior over the image patches and cannot do unconditional sampling  $x = T(z)$ .

The patchNR we used is given by the pre-trained model<sup>4</sup> trained on six images from LoDoPaB [76]. For PnP-ULA, we

<sup>4</sup><https://github.com/FabianAltekrueger/patchNR>

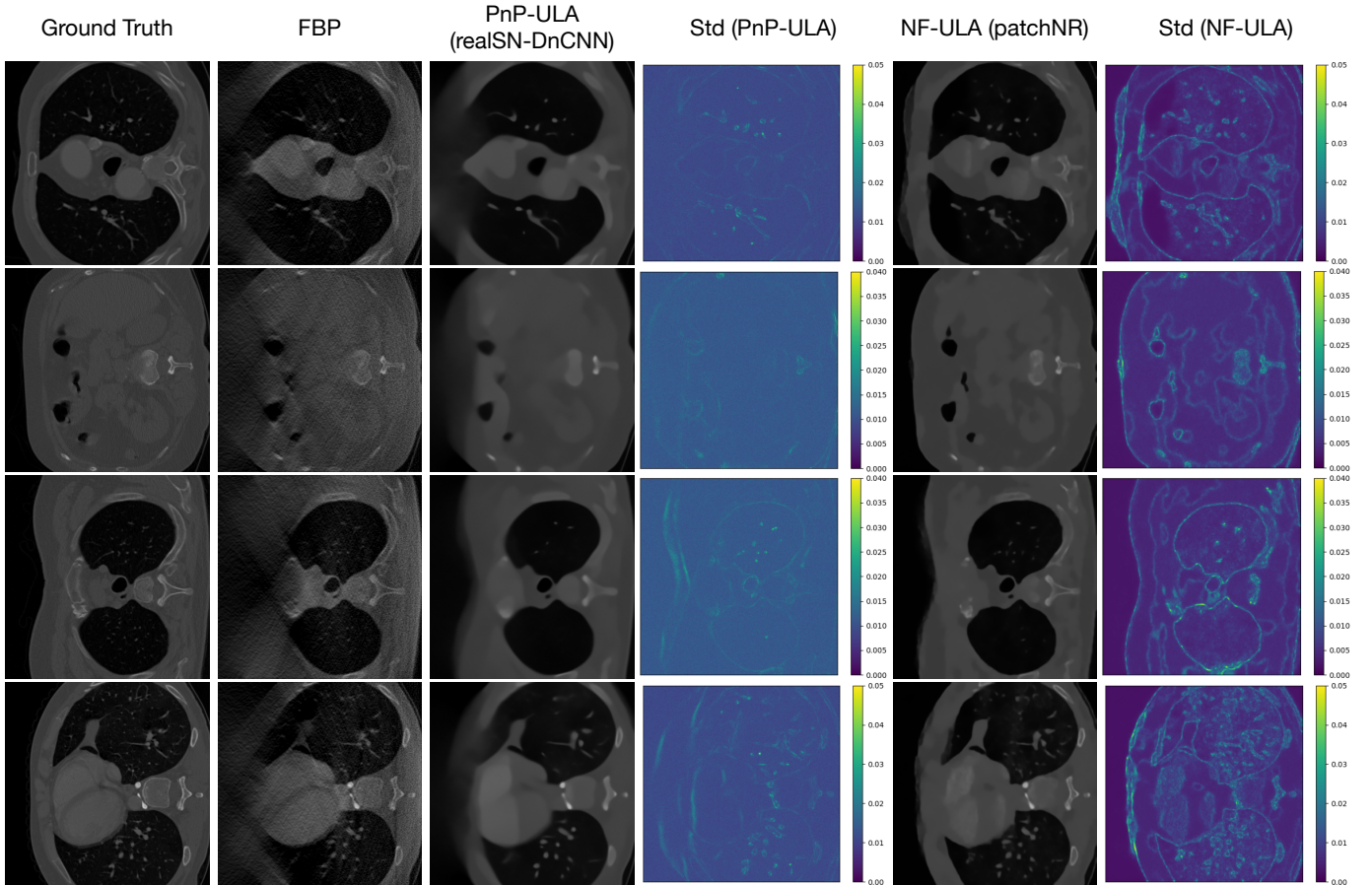


Fig. 6. CT reconstruction of Gaussian noise (limited angles). Column 1: Original image. Column 2: Filtered back projection (FBP). Column 3, 4: Posterior mean and the standard deviation of the samples generated by PnP-ULA (realSN-DnCNN). Column 5, 6: Posterior mean and the standard deviation of the samples generated by NF-ULA (patchNR). PSNR of the samples mean are provided in Table IV.

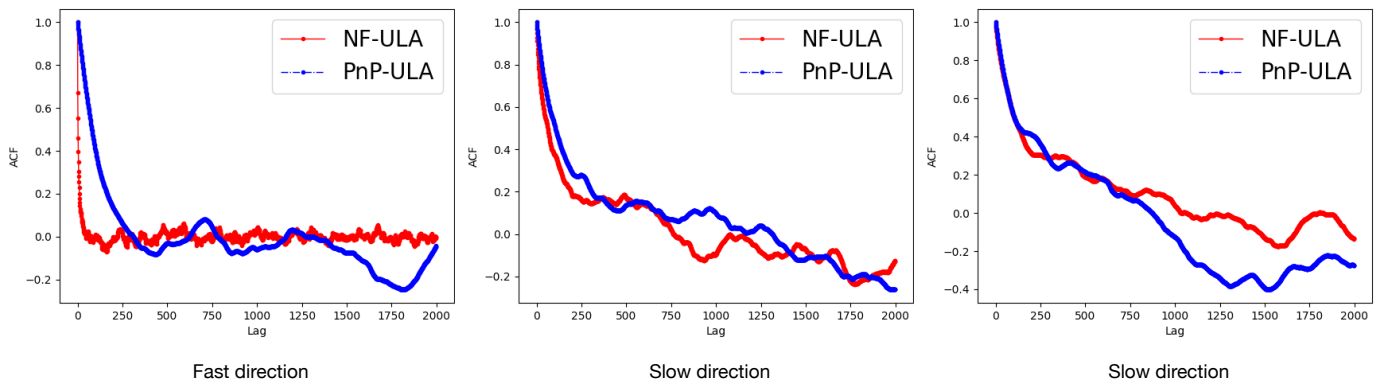


Fig. 7. The autocorrelation function (ACF) of the samples (Gaussian noise CT).

train the denoiser realSN-DnCNN on a 128-image subset of LoDoPaB, by adding Gaussian noise with the variance  $\varepsilon = (5/255)^2$  on the training data batches. We train a 17-layers realSN-DnCNN on the preprocessed image patches with size 40. The Lipschitz parameter of the realSN-DnCNN is set to 1. The patchNR has 2908880 parameters in total and the realSN-DnCNN has 556032 parameters.

**ULA parameters settings:** While in [60]  $\alpha = 700$  is the default setting,  $\alpha = 5000$  (Gaussian noise) works fine for NF-ULA. For PnP-ULA we set  $\alpha = 3$ . We use a smaller step-size

of both algorithms  $\delta = 1 \times 10^{-6}$  to ensure the convergence, since in CT reconstruction the forward operator  $A$  has larger norm. The convex set is set to be  $C = [-100, 100]^d$ . We initialize  $X_0$  as the filtered backprojection (FBP).

**Gaussian noise:** We first test the case with additive Gaussian noise. To be more specific, we use the following model

$$y = A(x) + n, \quad n \sim \sigma \mathcal{N}(0, I^m).$$

Since  $A(x) \in [0, 100]^{144 \times 512}$  is in a larger range, we select  $\sigma = 1.0$  to simulate the noisy sinogram  $y$ . Then the likelihood

can be easily calculated as

$$p(y|x) = \frac{1}{(2\pi\sigma^2)^{m/2}} \exp\left(-\frac{\|y - Ax\|^2}{2\sigma^2}\right). \quad (17)$$

To calculate  $\nabla \log p(y|x)$ , we also utilize the auto-gradient library in Pytorch to compute  $\nabla \|y - Ax\|^2$ . The reason is that in rare cases, there is some error in calculating the adjoint operator  $A^T$  since the adjoint of the Radon transform can only be implemented approximately in practice, therefore directly obtaining  $A^T(Ax - y)$  may not be accurate enough.

Since in the Poisson noise case the likelihood log gradient is not globally Lipschitz, the extra experiments with Poisson noise is moved to Appendix F.

**Behaviors of the algorithms:** We test PnP-ULA and NF-ULA on another 4 images from LoDoPaB [76], which are totally different from the 6 images trained by patchNR and 128 images trained by realSN-DnCNN. They are in the first column of Fig 6.

Both PnP-ULA and NF-ULA have a burn-in iterations more than 20000. Since we initialize  $X_0$  as FBP, the PSNR of  $X_n$  starts from around 21.90, slowly increases and is finally stable. Note that for different testing images, the burn-in time varies. For figure2 in Table IV, PnP-ULA has a 30000 burn-in iteration and then the PSNR of the samples never exceed 29, while for NF-ULA the PSNR of the samples keep increasing until 33, and finally the burn-in time for NF-ULA on figure2 is around 70000.

After the burn-in time, we calculate the posterior mean and the standard deviation by obtaining 10000 samples and compute the PSNR of the samples mean. For Gaussian noise, drawing 10000 samples by NF-ULA spend around 500 seconds and PnP-ULA spend 70 seconds. Thanks to the smaller network in patchNR, it saves large amount of time than Glow.

Fig 6 includes the original image, the FBP, the posterior mean and the standard deviation of PnP-ULA (realSN-DnCNN) and NF-ULA (patchNR). Simply looking at the posterior mean, PnP-ULA shows a worse reconstruction in the left area, due to the cut off angles and the extremely ill-posed problem. NF-ULA can recover the details well, which matches the results in the limited-angle CT in [60]. For standard deviation in the case of Gaussian noise, NF-ULA shows more realistic uncertainties than PnP-ULA on most areas, but still has huge uncertainties on left area. Table IV gives the PSNR of the posterior mean. NF-ULA obtain distinctly higher PSNR than PnP-ULA.

We also compare the ACF in Fig 7. We randomly select 100 dimensions among the total  $362 \times 362$  dimensions and compute the ACF on the 10000 samples. The ACF on the fast direction is similar to deblurring and inpainting: PnP-ULA decrease from 1 to 0 within 300 lags, while NF-ULA merely requires less than 50 lags. For slow directions, both two methods decrease to 0 more than 500 lags.

## V. CONCLUSION

In this paper, we introduce NF-ULA, a Langevin based Monte Carlo algorithm, which takes advantage of a normalizing flow for prior density estimation. The normalizing flow

can be pre-trained, thus it is compatible with different forward operators and inverse problems. Since NF-ULA only requires the log gradient of the prior, our algorithm still works in the cases where the normalizing flow can only evaluate the density but cannot do unconditional sampling. To guarantee that the posterior distribution is well-defined, we follow [51] to add a projection operator onto a bounded convex compact set, although in most cases the projection is not activated. We also prove the well-posedness of the posterior distribution that we aim to draw samples from. For the convergence of NF-ULA the most essential condition is still the Lipschitz drift, therefore we give a sufficient condition for the Lipschitz gradient of the log density of the normalizing flows. Moreover, we show that NF-ULA admits a invariant distribution, then we give a nonasymptotic bound of bias. We demonstrate our method by several Bayesian imaging experiments: image deblurring, image inpainting and limited-angle CT reconstruction. We show that better training of the normalizing flows leads to better samples and convergence of NF-ULA. Although currently NF-ULA has a longer sampling time because of the large network of normalizing flows, it has the potential to use better and smaller network to reduce the computation in future.

There are still some unanswered questions of NF-ULA. Although we give a sufficient condition when the gradient of the log density of normalizing flow is Lipschitz, the condition may be relaxed or even the equivalent condition might be possible. Moreover, given different curvature conditions on the drift other than Lipschitz, the studies of ULA on non-convex potentials have shown different convergence results and they can also be applied on NF-ULA. But this may require re-training the normalizing flows to enforce such conditions.

## ACKNOWLEDGMENTS

C-B. Schönlieb acknowledges support from the Philip Leverhulme Prize, the Royal Society Wolfson Fellowship, the EPSRC advanced career fellowship EP/V029428/1, EPSRC grants EP/S026045/1 and EP/T003553/1, EP/N014588/1, EP/T017961/1, the Wellcome Innovator Awards 215733/Z/19/Z and 221633/Z/20/Z, the European Union Horizon 2020 research and innovation programme under the Marie Skłodowska-Curie grant agreement No. 777826 NoMADS, the Cantab Capital Institute for the Mathematics of Information and the Alan Turing Institute.

## APPENDIX

### PROOFS

#### A. Proof of Lemma 1

*Proof.* For a constant  $R_0 > 0$ , let

$$B(0, R_0) := \{z \in \mathbb{R}^d : \|z\|_2 \leq R_0\}$$

be the closed ball of radius  $R_0$  centered at the origin. Since  $C \subset \mathbb{R}^d$  is compact, there exists  $R_0 > 0$  such that  $C \subset B(0, R_0)$ . Therefore, for all  $x \notin B(0, R_0)$ , it follows that

$$\|x - \Pi_C(x)\|_2 \geq \|x - \Pi_{B(0, R_0)}(x)\|_2 \geq \|x\|_2 - R_0 \geq 0.$$

Then, for all  $k \in \mathbb{N}$ , the following holds:

$$\begin{aligned} & \int_{\mathbb{R}^d \setminus B(0, R_0)} \|x\|^k \exp\left(-\frac{\|x - \Pi_C(x)\|_2^2}{2\lambda}\right) dx \\ & \leq \int_{\mathbb{R}^d \setminus B(0, R_0)} \|x\|^k \exp\left(-\frac{(\|x\|_2 - R_0)^2}{2\lambda}\right) dx \\ & \leq \int_{\mathbb{R}^d \setminus B(0, R_0)} \|x\|^k \exp\left(-\frac{\|x\|_2^2 - 2R_0}{4\lambda}\right) dx < +\infty, \end{aligned}$$

where the last inequality comes from that  $k$ -order moments of Gaussian distribution is finite.  $\square$

### B. Proof of Lemma 2

*Proof.* Since A 2 is satisfied, from Algorithm 1 and (11) we have that  $\nabla \log p_\lambda(x|y)$  is Lipschitz continuous if and only if  $\alpha \nabla \log q_\theta(x) + (\Pi_C(x) - x)/\lambda$  is Lipschitz continuous.

From [57], the operator  $(\text{Id} - \text{Prox}_{\iota_C})$  is firmly non-expansive, i.e.,  $\forall x, y \in \mathbb{R}^d$ ,

$$\begin{aligned} & \|(\Pi_C(x) - x) - (\Pi_C(y) - y)\|_2^2 \\ & \leq \langle (\Pi_C(x) - x) - (\Pi_C(y) - y), x - y \rangle \\ & \leq \|(\Pi_C(x) - x) - (\Pi_C(y) - y)\|_2 \|x - y\|_2. \end{aligned}$$

Therefore,  $(\Pi_C(x) - x)/\lambda$  is  $1/\lambda$ -Lipschitz. Hence, for any  $\alpha > 0$ ,  $\nabla \log p_\lambda(x|y)$  is Lipschitz-continuous if and only if  $\nabla \log q_\theta(x)$  is Lipschitz-continuous.  $\square$

### C. Proof of Proposition 2

*Proof.* Without loss of generality, assume that  $G$  is a composition of only one-layer affine coupling network. Since  $G_{<j}$  is independent of  $x_j$  and the diagonal of the Jacobian is  $(J_G(x))_{j,j} = \varphi_j(x_{<j})$ , from (5) we have that

$$\begin{aligned} & \log q_\theta(x) \\ & = \log q_z(G(x)) + \log |\det J_G(x)| \\ & = -\frac{1}{2} \|G(x)\|_2^2 + \log |\det J_{T_\theta^{-1}}(x)| + \text{const.} \\ & = -\frac{1}{2} \|G(x)\|_2^2 + \sum_{j=1}^d \log |\varphi_j(x_{<j})| + \text{const.} \end{aligned}$$

Taking the gradient on both sides and we get

$$\nabla \log q_\theta(x) = -(J_G(x))^T G(x) + \sum_{j=1}^d \nabla \log \varphi_j(x_{<j}). \quad (18)$$

Since  $\varphi_j$  is a constant function,  $\eta_j$  is Lipschitz and  $\forall i < j$ ,  $\frac{\partial \eta_j}{\partial x_i}$  is piecewise constant on  $\mathbb{R}$ , we have that  $\nabla \log \varphi_j = 0$  and  $(J_G(x))_{j,i} = \frac{\partial \eta_j}{\partial x_i}$ , which means that every element of  $J_G(x)$  is a bounded piecewise constant function of  $x$ . Then both  $G(x)$  and  $(J_G(x))^T G(x)$  are Lipschitz, therefore  $\nabla \log q_\theta(x)$  is Lipschitz.  $\square$

### D. Proof of Theorem 1

*Proof.* From A 3,  $b_\lambda(x)$  in (14) and that  $(\text{Id} - \Pi_C)/\lambda$  is  $1/\lambda$ -Lipschitz, we have that for any  $x_1, x_2 \in \mathbb{R}^d$ ,

$$\|b_\lambda(x_1) - b_\lambda(x_2)\|_2 \leq (L_y + \alpha L + 1/\lambda) \|x_1 - x_2\|_2.$$

Denote  $R_C = \sup \{\|x_1 - x_2\| : x_1, x_2 \in C\}$ . Since we have  $2\lambda(\alpha L - m) \leq 1$ , from (14) and the Cauchy-Schwarz inequality we have that for any  $x_1, x_2 \in \mathbb{R}^d$ ,

$$\begin{aligned} & \langle b_\lambda(x_1) - b_\lambda(x_2), x_1 - x_2 \rangle \\ & \leq (-m + \alpha L) \|x_1 - x_2\|^2 - \frac{\|x_1 - x_2\|^2}{\lambda} + \frac{R_C \|x_1 - x_2\|}{\lambda} \\ & \leq -\frac{\|x_1 - x_2\|^2}{2\lambda} + \frac{R_C \|x_1 - x_2\|}{\lambda}. \end{aligned} \quad (19)$$

For any  $x_1, x_2 \in \mathbb{R}^d$  satisfying  $\|x_1 - x_2\| \geq 4R_C$ , we obtain the contractivity at infinity condition on the drift  $b_\lambda$

$$\langle b_\lambda(x_1) - b_\lambda(x_2), x_1 - x_2 \rangle \leq -\frac{\|x_1 - x_2\|^2}{4\lambda}, \quad (20)$$

which indicates the strongly convexity at infinity.

After simple computation by letting  $x_2 = 0$  in (19), we also have that for any  $x \in \mathbb{R}^d$ ,

$$\begin{aligned} & \langle b_\lambda(x), x \rangle \leq -\|x\|^2/(4\lambda) \\ & + \sup_{\tilde{x} \in \mathbb{R}^d} \{(R_C/\lambda + \|b_\lambda(0)\|) \|\tilde{x}\| - \|\tilde{x}\|^2/(4\lambda)\}. \end{aligned} \quad (21)$$

Let  $\bar{\gamma} = (4\lambda)^{-1} (L_y + \alpha L + 1/\lambda)^{-2}$ . From (21), using Lemma SM5.1 in [62] and we get that there exist  $\lambda_V \in (0, 1]$ ,  $c \geq 0$  such that for any  $\delta \in (0, \bar{\gamma}]$ ,  $R_\delta$  satisfies the discrete drift condition  $\mathbf{D}_d(V, \lambda_V^\delta, c\delta)$ . Since  $\bar{\delta} \leq \bar{\gamma}$  and the contractivity condition (20) holds, then from Theorem 8 and Corollary 2 in [48], we can find  $A_2 \geq 0$  and  $\rho_2 \in [0, 1)$  such that for any  $\delta \in (0, \bar{\delta}]$ ,  $x_1, x_2 \in \mathbb{R}^d$ , and  $k \in \mathbb{N}$ ,

$$\begin{aligned} & \|\delta_{x_1} R_\delta^k - \delta_{x_2} R_\delta^k\|_{\text{TV}} \leq A_2 \rho_2^{k\delta} (V(x_1) + V(x_2)) \\ & \leq A_2 \rho_2^{k\delta} (V^2(x_1) + V^2(x_2)) \quad (22) \\ & \mathbf{W}_1(\delta_{x_1} R_\delta^k, \delta_{x_2} R_\delta^k) \leq A_2 \rho_2^{k\delta} \|x_1 - x_2\|_2. \end{aligned}$$

For any probability measure  $\nu_1, \nu_2$ , from the definition (12) and Hölder's inequality we have that

$$\|\nu_1 - \nu_2\|_V \leq \|\nu_1 - \nu_2\|_{\text{TV}}^{1/2} (\nu_1[V^2] + \nu_2[V^2])^{1/2}. \quad (23)$$

Then we conclude the proof.  $\square$

### E. Proof of Theorem 2

*Proof.* Most of our proof is based on [62] and [48].

Recall that

$$\begin{aligned} & R_\delta(x, A) \\ & = (2\pi)^{-d/2} \int_{\mathbb{R}^d} \mathbf{1}_A\left(x + \delta b_\lambda(x) + \sqrt{2\delta}z\right) \exp[-\|z\|^2/2] dz. \end{aligned} \quad (24)$$

We introduce the stochastic process  $(\bar{\mathbf{X}}_t)_{t \geq 0}$ , which is exactly the solution of the following SDE:

$$\begin{cases} d\bar{\mathbf{X}}_t = b_\lambda(\bar{\mathbf{X}}_t) dt + \sqrt{2} d\mathbf{B}_t \\ b_\lambda(x) = \nabla \log(p(y|x)) + \alpha \nabla \log q_\theta(x) + \frac{\Pi_C(x) - x}{\lambda} \\ \bar{\mathbf{X}}_0 = X_0 \end{cases} \quad (25)$$

where  $(\mathbf{B}_t)_{t \geq 0}$  is a  $d$ -dimensional Brownian motion.

From Lemma 2,  $b_\lambda$  is  $(L_y + \alpha L + 1/\lambda)$ -Lipschitz continuous. From Chapter 5, Theorem 2.9 of [64] we have that the SDE (25) admits a unique strong solution for any initial condition  $\bar{\mathbf{X}}_0$  with  $\mathbb{E}[\|\bar{\mathbf{X}}_0\|^2] < +\infty$ . We denote by  $(P_t)_{t \geq 0}$  the semigroup associated with the strong solutions of SDE (25). Similarly to the proof of Theorem 1, replacing Corollary 2 in [48] by Theorem 21 and Corollary 22 in [48], there exist  $\tilde{A}_1 \geq 0$  and  $\tilde{\rho}_1 \in [0, 1)$  such that that for any  $x_1, x_2 \in \mathbb{R}^d$  and  $t \geq 0$ ,

$$\begin{aligned} \|\delta_{x_1} P_t - \delta_{x_2} P_t\|_V &\leq \tilde{A}_1 \tilde{\rho}_1^t (V^2(x_1) + V^2(x_2)), \\ \mathbf{W}_1(\delta_{x_1} P_t, \delta_{x_2} P_t) &\leq \tilde{A}_1 \tilde{\rho}_1^t \|x_1 - x_2\|_2. \end{aligned} \quad (26)$$

Combining (26), Theorem 1, the fact that  $(\mathcal{P}_1(\mathbb{R}^d), \mathbf{W}_1)$  is a complete metric space and the Picard fixed point theorem, we can obtain that for any  $\delta \in (0, \bar{\delta}]$  there exist  $\pi_{\delta, \lambda}, \tilde{\pi}_\lambda \in \mathcal{P}_1(\mathbb{R}^d)$  such that  $\pi_{\delta, \lambda} R_\delta = \pi_{\delta, \lambda}$  and for any  $t \geq 0$ ,  $\tilde{\pi}_\lambda P_t = \tilde{\pi}_\lambda$ . By Theorem 2.1 in [37] we have that for any  $x \in \mathbb{R}^d$ ,

$$(d\tilde{\pi}_\lambda/d\text{Leb})(x) \propto \exp[-\iota_C^{(\lambda)}(x)] p(y|x) p_\lambda^\alpha(x), \quad (27)$$

Therefore from (10)  $\pi_\lambda$  and  $\tilde{\pi}_\lambda$  are exactly the same.

Similar to (15), from (26) we have that for any  $t \geq 0$  and  $x \in \mathbb{R}^d$ ,

$$\|\delta_x P_t - \pi_\lambda\|_V \leq \tilde{A}_1 \tilde{\rho}_1^t \left( V^2(x) + \int_{\mathbb{R}^d} V^2(\tilde{x}) d\pi_\lambda(\tilde{x}) \right) \quad (28)$$

Since we already proved that  $\int_{\mathbb{R}^d} V^2(\tilde{x}) d\pi_\lambda(\tilde{x}) < +\infty$  in Lemma 1, we can find  $B_1 \geq 0$  such that for any  $x \in \mathbb{R}^d$  we have

$$\|\delta_x P_t - \pi_\lambda\|_V \leq B_1 \tilde{\rho}_1^t V^2(x). \quad (29)$$

To compare  $\pi_{\delta, \lambda}$  with  $\pi_\delta$ , we first construct a continuous time Markov process  $X_t^{(1)}$  such that  $X_{j/m}^{(1)}$  has the same distribution as the  $j$ -th sample  $X_j$  by NF-ULA (11).

Select a large  $m \in \mathbb{N}^*$  such that  $m \geq \bar{\delta}^{-1}$ . Let's now consider the interval  $[0, l]$ ,  $l \in \mathbb{N}^*$  and define  $b_1(t, (w_t)_{t \in [0, l]}) = \sum_{j=0}^{ml-1} \mathbf{1}_{[j/m, (j+1)/m)}(t) b_\lambda(w_{j\delta})$  and  $b_2(t, (w_t)_{t \in [0, l]}) = b_\lambda(w_t)$ . Let  $\mathbf{X}_t^{(1)}$  and  $\mathbf{X}_t^{(2)}$  be the unique strong solution of SDE  $d\mathbf{X}_t = b(t, (\mathbf{X}_t)_{t \in [0, l]}) dt + \sqrt{2} d\mathbf{B}_t$  with  $\mathbf{X}_0 = x \in \mathbb{R}^d$  and  $b = b_1$ , respectively  $b = b_2$ . Note that  $(\mathbf{X}_{k/m}^{(1)}) = (X_k)_{k \in \mathbb{N}}$  and  $(\mathbf{X}_t^{(2)})_{t \geq 0} = (\bar{\mathbf{X}}_t)_{t \geq 0}$ . Denote  $P_t^{(1)}$  and  $P_t^{(2)}$  the Markov semigroup associated with  $\mathbf{X}_t^{(1)}$  and  $\mathbf{X}_t^{(2)}$ . Then for any  $x \in \mathbb{R}^d$ ,  $k \in \mathbb{N}^*$  we have

$$\delta_x R_{1/m}^{km} = \delta_x P_k^{(1)}, \quad \delta_x P_k = \delta_x P_k^{(2)}. \quad (30)$$

From Lemma 2 and A 3, for any  $t \in [j/m, (j+1)/m)$ ,  $j \in \{0, \dots, ml-1\}$  and  $(w_t)_{t \in [0, l]} \in C([0, l], \mathbb{R}^d)$  we have that

$$\begin{aligned} &\left\| b_1\left(t, (w_t)_{t \in [0, l]}\right) - b_2\left(t, (w_t)_{t \in [0, l]}\right) \right\|^2 \\ &= \left\| b_\lambda(w_{j/m}) - b_\lambda(w_t) \right\|^2 \\ &\leq (L_y + \alpha L + 1/\lambda)^2 \|w_{j/m} - w_t\|^2. \end{aligned} \quad (31)$$

Using Itô's isometry we have for any  $t \in [j/m, (j+1)/m)$ ,

$$\begin{aligned} \mathbb{E} \left[ \left\| \mathbf{X}_t^{(1)} - \mathbf{X}_{j/m}^{(1)} \right\|^2 \right] &= \mathbb{E} \left[ \left\| \int_{j/m}^t \sqrt{2} d\mathbf{B}_\tau \right\|^2 \right] \\ &= 2d \mathbb{E} \left( \int_{j/m}^t d\tau \right) \leq \frac{2d}{m}. \end{aligned} \quad (32)$$

Then from (31), for  $i \in \{0, \dots, l-1\}$  we have that

$$\begin{aligned} &\int_i^{i+1} \mathbb{E} \left[ \left\| b_1\left(t, \mathbf{X}_t^{(1)}\right) - b_2\left(t, \mathbf{X}_t^{(1)}\right) \right\|^2 \right] dt \\ &\leq 2(L_y + \alpha L + 1/\lambda)^2 d/m. \end{aligned} \quad (33)$$

From (30) and Lemma SM6.1 in [62], we obtain that there exists  $B_b \geq 0$  such that for any  $x \in \mathbb{R}^d$ ,

$$\begin{aligned} &\left\| \delta_x R_{1/m}^{lm} - \delta_x P_l \right\|_V = \left\| \delta_x P_l^{(1)} - \delta_x P_l^{(2)} \right\|_V \\ &\leq \left( \delta_x P_l^{(1)} [V^2] + \delta_x P_l^{(2)} [V^2] \right)^{1/2} \times \\ &\quad \left( \sum_{i=0}^{l-1} \int_i^{i+1} \mathbb{E} \left[ \left\| b_1\left(t, \mathbf{X}_t^{(1)}\right) - b_2\left(t, \mathbf{X}_t^{(1)}\right) \right\|^2 \right] dt \right)^{1/2} \\ &\leq B_b \sqrt{\frac{l}{m}} \left( \delta_x P_t^{(1)} [V^2] + \delta_x P_t^{(2)} [V^2] \right)^{1/2}, \end{aligned} \quad (34)$$

where  $B_b = (L_y + \alpha L + 1/\lambda) \sqrt{2d}$ .

Assume that there is a function  $W \in C^2(\mathbb{R}^d, [1, +\infty))$  such that  $\lim_{\|x\| \rightarrow +\infty} W(x) = +\infty$ . Recall that from (21), using Lemma SM5.1 in [62] and we get that there exist  $\lambda_W \in (0, 1]$ ,  $c, \beta \geq 0$  and  $\zeta > 0$  such that for any  $\delta \in \left(0, (4\lambda)^{-1} (L_y + \alpha L + 1/\lambda)^{-2}\right]$ ,  $R_\delta$  satisfies the discrete drift condition  $\mathbf{D}_d(W, \lambda_W^\delta, c\delta)$  and  $(P_t)_{t \geq 0}$  satisfies the continuous drift condition  $\mathbf{D}_c(W, \zeta, \beta)$ . From Lemma SM5.2 in [62], there exists  $B_c \geq 0$  such that for any  $x \in \mathbb{R}^d$ ,  $t \geq 0$  and  $k \in \mathbb{N}^*$  we have

$$R_\delta^k W(x) + P_t W(x) \leq B_c^2 W(x). \quad (35)$$

Let  $W(x) = V^2(x)$  and  $k = ml$ ,  $\delta = 1/m$ ,  $t = l$ , then  $\forall x \in \mathbb{R}^d$ ,

$$\delta_x P_l^{(1)} [V^2] + \delta_x P_l^{(2)} [V^2] \leq B_c^2 V^2(x) \quad (36)$$

Combined with (34), we have that

$$\left\| \delta_x R_{1/m}^{ml} - \delta_x P_l \right\|_V \leq B_b B_c V(x) \sqrt{\frac{l}{m}} \quad (37)$$

To give a bound on  $\left\| \delta_x R_{1/m}^{ml} - \pi_\lambda \right\|_V$ , we use triangular inequality to split it into two terms:

$$\left\| \delta_x R_{1/m}^{ml} - \pi_\lambda \right\|_V \leq \left\| \delta_x R_{1/m}^{ml} - \delta_x P_l \right\|_V + \left\| \delta_x P_l - \pi_\lambda \right\|_V. \quad (38)$$

TABLE V  
CT RECONSTRUCTION OF POISSON NOISE, LIMITED ANGLES.

CT	network	parameters	$C$	PSNR
figure1				
NF-ULA	PatchNR	$\alpha = 4000$	$[-100, 100]^d$	29.88
PnP-ULA	realSN-DnCNN	$\alpha = 3$	$[-100, 100]^d$	26.93
figure2				
NF-ULA	PatchNR	$\alpha = 4000$	$[-100, 100]^d$	33.85
PnP-ULA	realSN-DnCNN	$\alpha = 3$	$[-100, 100]^d$	27.78
figure3				
NF-ULA	PatchNR	$\alpha = 4000$	$[-100, 100]^d$	31.10
PnP-ULA	realSN-DnCNN	$\alpha = 3$	$[-100, 100]^d$	29.64
figure4				
NF-ULA	PatchNR	$\alpha = 4000$	$[-100, 100]^d$	30.67
PnP-ULA	realSN-DnCNN	$\alpha = 3$	$[-100, 100]^d$	27.01

Using this result and (29), we obtain that there exists  $B_1, B_2 \geq 0$  such that for any  $m \in \mathbb{N}^*$  with  $1/m \leq \bar{\delta}$ ,

$$\left\| \delta_x R_{1/m}^{ml} - \pi_\lambda \right\|_V \leq B_1 \tilde{\rho}_1^l V^2(x) + B_2 V(x) \sqrt{\frac{l}{m}}. \quad (39)$$

The proof in the general case where  $\delta \in (0, \bar{\delta})$  is similar when the interval  $[0, l]$  is changed to  $[0, lm\delta]$ .

Then we obtain that there exists  $B_1, B_2 \geq 0$ ,  $\tilde{\rho}_1 \in [0, 1]$  such that for any  $\delta \in (0, \bar{\delta})$ ,  $k \in \mathbb{N}^*$ ,

$$\left\| \delta_x R_\delta^k - \pi_\lambda \right\|_V \leq B_1 \tilde{\rho}_1^{k\delta} V^2(x) + B_2 V(x) \sqrt{\delta^2 k}. \quad (40)$$

□

## EXTRA EXPERIMENTS

### F. CT reconstruction of Poisson noise

The second limited-angle CT reconstruction experiment we test is using the Poisson noise, where the model can be formulated as

$$y = A(x) + n, \quad n = -A(x) - \frac{1}{\mu} \log \left( \frac{N_1}{N_0} \right),$$

and we simulate the noisy sinogram as

$$N_1 \sim \text{Poisson}(N_0 \exp(-A(x)\mu)).$$

Here  $N_0 = 4096$  is the mean photon count per detector bin without attenuation.  $\mu = 0.05$  is a constant. Since Poisson noise implies a different likelihood

$$p(y|x) = \frac{1}{K_0} \exp(-J(x, y)),$$

$$J(x, y) = \sum_{i=1}^m e^{-A(x)_i \mu} N_0 + e^{-y_i \mu} N_0 (A(x)_i \mu - \log(N_0)),$$

we calculate  $\nabla \log p(y|x) = -\nabla J(x, y)$  by using the auto-gradient library.

We select a different  $\alpha = 4000$  for NF-ULA, while keeping all the other settings the same as in Sec. IV-C.

Both PnP-ULA and NF-ULA have a burn-in iterations more than 20000. After the burn-in time, we calculate the posterior mean and the standard deviation by obtaining 10000 samples and compute the PSNR of the samples mean. For Poisson noise the likelihood is more complicated than Gaussian, and NF-ULA spend 510s.

Fig 8 includes the original image, the FBP, the posterior mean and the standard deviation of PnP-ULA (realSN-DnCNN) and NF-ULA (patchNR). Table V provides the PSNR of the posterior mean. Note that the huge uncertainties of standard deviation on the left area in Fig 6 is slightly alleviated in the Poisson noise experiments.

## REFERENCES

- [1] S. Arridge, P. Maass, O. Öktem, and C.-B. Schönlieb, "Solving inverse problems using data-driven models," *Acta Numerica*, vol. 28, pp. 1–174, 2019.
- [2] G. Ongie, A. Jalal, C. A. Metzler, R. G. Baraniuk, A. G. Dimakis, and R. Willett, "Deep learning techniques for inverse problems in imaging," *IEEE Journal on Selected Areas in Information Theory*, vol. 1, no. 1, pp. 39–56, 2020.
- [3] A. Chambolle, V. Caselles, D. Cremers, M. Novaga, and T. Pock, "An introduction to total variation for image analysis," *Theoretical foundations and numerical methods for sparse recovery*, vol. 9, no. 263–340, p. 227, 2010.
- [4] S. V. Venkatakrishnan, C. A. Bouman, and B. Wohlberg, "Plug-and-play priors for model based reconstruction," in *2013 IEEE Global Conference on Signal and Information Processing*. IEEE, 2013, pp. 945–948.
- [5] P. L. Combettes and J.-C. Pesquet, "Proximal splitting methods in signal processing," *Fixed-point algorithms for inverse problems in science and engineering*, pp. 185–212, 2011.
- [6] O. Ronneberger, P. Fischer, and T. Brox, "U-net: Convolutional networks for biomedical image segmentation," in *Medical Image Computing and Computer-Assisted Intervention—MICCAI 2015: 18th International Conference, Munich, Germany, October 5–9, 2015, Proceedings, Part III 18*. Springer, 2015, pp. 234–241.
- [7] K. H. Jin, M. T. McCann, E. Froustey, and M. Unser, "Deep convolutional neural network for inverse problems in imaging," *IEEE Transactions on Image Processing*, vol. 26, no. 9, pp. 4509–4522, 2017.
- [8] K. Zhang, Y. Li, W. Zuo, L. Zhang, L. Van Gool, and R. Timofte, "Plug-and-play image restoration with deep denoiser prior," *IEEE Transactions on Pattern Analysis and Machine Intelligence*, vol. 44, no. 10, pp. 6360–6376, 2021.
- [9] Y. Romano, M. Elad, and P. Milanfar, "The little engine that could: Regularization by denoising (red)," *SIAM Journal on Imaging Sciences*, vol. 10, no. 4, pp. 1804–1844, 2017.
- [10] J. Hertrich, S. Neumayer, and G. Steidl, "Convolutional proximal neural networks and plug-and-play algorithms," *Linear Algebra and its Applications*, vol. 631, pp. 203–234, 2021.
- [11] D. Gilton, G. Ongie, and R. Willett, "Learned patch-based regularization for inverse problems in imaging," in *2019 IEEE 8th International Workshop on Computational Advances in Multi-Sensor Adaptive Processing (CAMSAP)*. IEEE, 2019, pp. 211–215.
- [12] S. Sreehari, S. V. Venkatakrishnan, B. Wohlberg, G. T. Buzzard, L. F. Drummy, J. P. Simmons, and C. A. Bouman, "Plug-and-play priors for bright field electron tomography and sparse interpolation," *IEEE Transactions on Computational Imaging*, vol. 2, no. 4, pp. 408–423, 2016.
- [13] H. Y. Tan, S. Mukherjee, J. Tang, and C.-B. Schönlieb, "Provably convergent plug-and-play quasi-newton methods," *arXiv preprint arXiv:2303.07271*, 2023.
- [14] J. Adler and O. Öktem, "Learned primal-dual reconstruction," *IEEE transactions on medical imaging*, vol. 37, no. 6, pp. 1322–1332, 2018.
- [15] Y. Song, L. Shen, L. Xing, and S. Ermon, "Solving inverse problems in medical imaging with score-based generative models," *arXiv preprint arXiv:2111.08005*, 2021.
- [16] X. Pan, X. Zhan, B. Dai, D. Lin, C. C. Loy, and P. Luo, "Exploiting deep generative prior for versatile image restoration and manipulation," *IEEE Transactions on Pattern Analysis and Machine Intelligence*, vol. 44, no. 11, pp. 7474–7489, 2021.
- [17] M. Asim, M. Daniels, O. Leong, A. Ahmed, and P. Hand, "Invertible generative models for inverse problems: mitigating representation error and dataset bias," in *International Conference on Machine Learning*. PMLR, 2020, pp. 399–409.
- [18] J. Whang, Q. Lei, and A. Dimakis, "Solving inverse problems with a flow-based noise model," in *International Conference on Machine Learning*. PMLR, 2021, pp. 11 146–11 157.
- [19] S. Hurault, A. Leclaire, and N. Papadakis, "Gradient step denoiser for convergent plug-and-play," *arXiv preprint arXiv:2110.03220*, 2021.

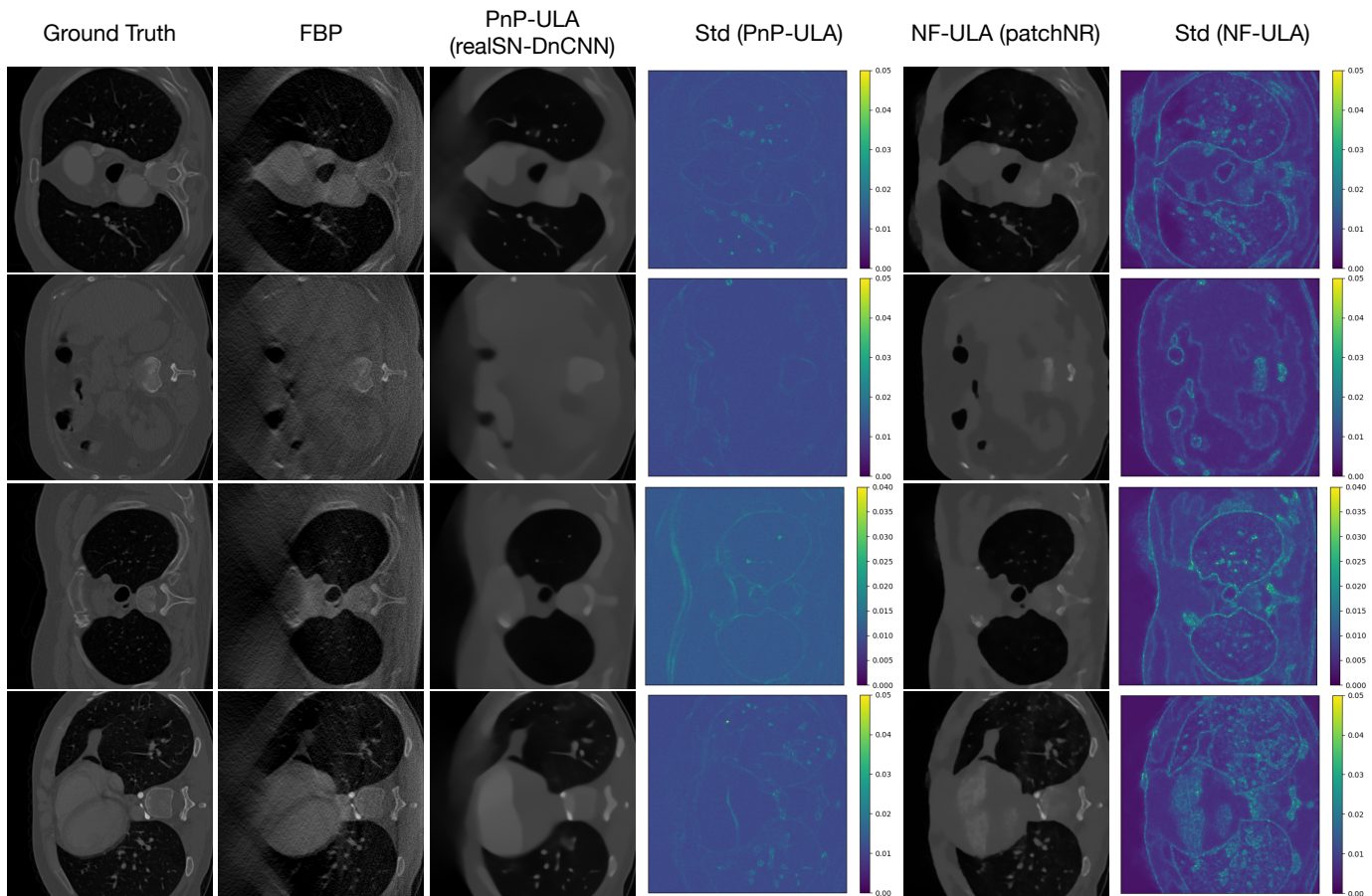


Fig. 8. CT reconstruction of Poisson noise (limited angles). Column 1: Original image. Column 2: Filtered back projection (FBP). Column 3, 4: Posterior mean and the standard deviation of the samples generated by PnP-ULA (realSN-DnCNN). Column 5, 6: Posterior mean and the standard deviation of the samples generated by NF-ULA (patchNR). PSNR of the samples mean are provided in Table V.

- [20] E. Kobler, A. Effland, K. Kunisch, and T. Pock, “Total deep variation: A stable regularization method for inverse problems,” *IEEE transactions on pattern analysis and machine intelligence*, vol. 44, no. 12, pp. 9163–9180, 2021.
- [21] S. Lunz, O. Öktem, and C.-B. Schönlieb, “Adversarial regularizers in inverse problems,” *Advances in neural information processing systems*, vol. 31, 2018.
- [22] S. Mukherjee, M. Carioni, O. Öktem, and C.-B. Schönlieb, “End-to-end reconstruction meets data-driven regularization for inverse problems,” *Advances in Neural Information Processing Systems*, vol. 34, pp. 21 413–21 425, 2021.
- [23] J. Prost, A. Houdard, A. Almansa, and N. Papadakis, “Learning local regularization for variational image restoration,” in *Scale Space and Variational Methods in Computer Vision: 8th International Conference, SSVN 2021, Virtual Event, May 16–20, 2021, Proceedings*. Springer, 2021, pp. 358–370.
- [24] S. Mukherjee, S. Dittmer, Z. Shumaylov, S. Lunz, O. Öktem, and C.-B. Schönlieb, “Learned convex regularizers for inverse problems,” *arXiv preprint arXiv:2008.02839*, 2020.
- [25] B. Amos, L. Xu, and J. Z. Kolter, “Input convex neural networks,” in *International Conference on Machine Learning*. PMLR, 2017, pp. 146–155.
- [26] A. M. Stuart, “Inverse problems: a bayesian perspective,” *Acta numerica*, vol. 19, pp. 451–559, 2010.
- [27] J. Kaipio and E. Somersalo, *Statistical and computational inverse problems*. Springer Science & Business Media, 2006, vol. 160.
- [28] A. Tarantola, *Inverse problem theory and methods for model parameter estimation*. SIAM, 2005.
- [29] C. Louchet and L. Moisan, “Posterior expectation of the total variation model: properties and experiments,” *SIAM Journal on Imaging Sciences*, vol. 6, no. 4, pp. 2640–2684, 2013.
- [30] M. Pereyra, “Proximal markov chain monte carlo algorithms,” *Statistics and Computing*, vol. 26, no. 4, pp. 745–760, 2016.
- [31] D. Zoran and Y. Weiss, “From learning models of natural image patches to whole image restoration,” in *2011 international conference on computer vision*. IEEE, 2011, pp. 479–486.
- [32] G. Yu, G. Sapiro, and S. Mallat, “Solving inverse problems with piecewise linear estimators: From gaussian mixture models to structured sparsity,” *IEEE Transactions on Image Processing*, vol. 21, no. 5, pp. 2481–2499, 2011.
- [33] C. Aguerreberre, A. Almansa, J. Delon, Y. Gousseau, and P. Musé, “A bayesian hyperprior approach for joint image denoising and interpolation, with an application to hdr imaging,” *IEEE Transactions on Computational Imaging*, vol. 3, no. 4, pp. 633–646, 2017.
- [34] A. Houdard, C. Bouveyron, and J. Delon, “High-dimensional mixture models for unsupervised image denoising (hdmi),” *SIAM Journal on Imaging Sciences*, vol. 11, no. 4, pp. 2815–2846, 2018.
- [35] W. R. Gilks, S. Richardson, and D. Spiegelhalter, *Markov chain Monte Carlo in practice*. CRC press, 1995.
- [36] R. Neal, “Bayesian learning via stochastic dynamics,” *Advances in neural information processing systems*, vol. 5, 1992.
- [37] G. O. Roberts and R. L. Tweedie, “Exponential convergence of langevin distributions and their discrete approximations,” *Bernoulli*, pp. 341–363, 1996.
- [38] A. S. Dalalyan, “Theoretical guarantees for approximate sampling from smooth and log-concave densities,” *Journal of the Royal Statistical Society: Series B (Statistical Methodology)*, vol. 79, no. 3, pp. 651–676, 2017.
- [39] A. Durmus and E. Moulines, “Nonasymptotic convergence analysis for the unadjusted langevin algorithm,” *The Annals of Applied Probability*, vol. 27, no. 3, pp. 1551–1587, 2017.
- [40] A. S. Dalalyan and A. Karagulyan, “User-friendly guarantees for the langevin monte carlo with inaccurate gradient,” *Stochastic Processes*

- and their Applications, vol. 129, no. 12, pp. 5278–5311, 2019.
- [41] A. Durmus, S. Majewski, and B. Miasojedow, “Analysis of langevin monte carlo via convex optimization,” *The Journal of Machine Learning Research*, vol. 20, no. 1, pp. 2666–2711, 2019.
- [42] A. Durmus, E. Moulines, and M. Pereyra, “Efficient bayesian computation by proximal markov chain monte carlo: when langevin meets moreau,” *SIAM Journal on Imaging Sciences*, vol. 11, no. 1, pp. 473–506, 2018.
- [43] A. Salim, D. Kovalev, and P. Richtárik, “Stochastic proximal langevin algorithm: Potential splitting and nonasymptotic rates,” *Advances in Neural Information Processing Systems*, vol. 32, 2019.
- [44] J. Lehec, “The langevin monte carlo algorithm in the non-smooth log-concave case,” *arXiv preprint arXiv:2101.10695*, 2021.
- [45] T. D. Luu, J. Fadili, and C. Chesneau, “Sampling from non-smooth distributions through langevin diffusion,” *Methodology and Computing in Applied Probability*, vol. 23, no. 4, pp. 1173–1201, 2021.
- [46] W. Mou, N. Flammarion, M. J. Wainwright, and P. L. Bartlett, “An efficient sampling algorithm for non-smooth composite potentials,” *Journal of Machine Learning Research*, vol. 23, no. 233, pp. 1–50, 2022.
- [47] X. Cheng, N. S. Chatterji, Y. Abbasi-Yadkori, P. L. Bartlett, and M. I. Jordan, “Sharp convergence rates for langevin dynamics in the nonconvex setting,” *arXiv preprint arXiv:1805.01648*, 2018.
- [48] V. De Bortoli and A. Durmus, “Convergence of diffusions and their discretizations: from continuous to discrete processes and back,” *arXiv preprint arXiv:1904.09808*, 2019.
- [49] M. B. Majka, A. Mijatović, and Łukasz Szpruch, “Nonasymptotic bounds for sampling algorithms without log-concavity,” *The Annals of Applied Probability*, vol. 30, no. 4, pp. 1534 – 1581, 2020.
- [50] M. A. Erdogdu and R. Hosseinzadeh, “On the convergence of langevin monte carlo: The interplay between tail growth and smoothness,” in *Conference on Learning Theory*. PMLR, 2021, pp. 1776–1822.
- [51] R. Laumont, V. D. Bortoli, A. Almansa, J. Delon, A. Durmus, and M. Pereyra, “Bayesian imaging using plug & play priors: when langevin meets tweedie,” *SIAM Journal on Imaging Sciences*, vol. 15, no. 2, pp. 701–737, 2022.
- [52] E. Ryu, J. Liu, S. Wang, X. Chen, Z. Wang, and W. Yin, “Plug-and-play methods provably converge with properly trained denoisers,” in *International Conference on Machine Learning*. PMLR, 2019, pp. 5546–5557.
- [53] D. Rezende and S. Mohamed, “Variational inference with normalizing flows,” in *International conference on machine learning*. PMLR, 2015, pp. 1530–1538.
- [54] L. Dinh, J. Sohl-Dickstein, and S. Bengio, “Density estimation using real nvp,” *arXiv preprint arXiv:1605.08803*, 2016.
- [55] G. Papamakarios, E. T. Nalisnick, D. J. Rezende, S. Mohamed, and B. Lakshminarayanan, “Normalizing flows for probabilistic modeling and inference,” *J. Mach. Learn. Res.*, vol. 22, no. 57, pp. 1–64, 2021.
- [56] D. P. Kingma and P. Dhariwal, “Glow: Generative flow with invertible 1x1 convolutions,” *Advances in neural information processing systems*, vol. 31, 2018.
- [57] H. H. Bauschke, P. L. Combettes *et al.*, *Convex analysis and monotone operator theory in Hilbert spaces*. Springer, 2011, vol. 408.
- [58] P. L. Combettes and V. R. Wajs, “Signal recovery by proximal forward-backward splitting,” *Multiscale Modeling & Simulation*, vol. 4, no. 4, pp. 1168–1200, 2005.
- [59] B. Efron, “Tweedie’s formula and selection bias,” *Journal of the American Statistical Association*, vol. 106, no. 496, pp. 1602–1614, 2011.
- [60] F. Altekruiger, A. Denker, P. Hagemann, J. Hertrich, P. Maass, and G. Steidl, “Patchnr: Learning from very few images by patch normalizing flow regularization,” *arXiv preprint arXiv:2205.12021*, 2022.
- [61] S. P. Meyn and R. L. Tweedie, “Stability of markovian processes iii: Foster–lyapunov criteria for continuous-time processes,” *Advances in Applied Probability*, vol. 25, no. 3, pp. 518–548, 1993.
- [62] R. Laumont, V. D. Bortoli, A. Almansa, J. Delon, A. Durmus, and M. Pereyra, “Supplementary materials: Bayesian imaging using plug & play priors: when langevin meets tweedie,” [https://epubs.siam.org/doi/suppl/10.1137/21M1406349/suppl\\_file/M140634\\_01.pdf](https://epubs.siam.org/doi/suppl/10.1137/21M1406349/suppl_file/M140634_01.pdf), 2022.
- [63] N. Ikeda and S. Watanabe, *Stochastic differential equations and diffusion processes*. Elsevier, 2014.
- [64] I. Karatzas, I. Karatzas, S. Shreve, and S. E. Shreve, *Brownian motion and stochastic calculus*. Springer Science & Business Media, 1991, vol. 113.
- [65] I. Kobyzev, S. J. Prince, and M. A. Brubaker, “Normalizing flows: An introduction and review of current methods,” *IEEE transactions on pattern analysis and machine intelligence*, vol. 43, no. 11, pp. 3964–3979, 2020.
- [66] A. Verine, B. Negrevergne, F. Rossi, and Y. Chevaleyre, “On the expressivity of bi-lipschitz normalizing flows,” *arXiv preprint arXiv:2107.07232*, 2021.
- [67] P. Jaini, I. Kobyzev, Y. Yu, and M. Brubaker, “Tails of lipschitz triangular flows,” in *International Conference on Machine Learning*. PMLR, 2020, pp. 4673–4681.
- [68] L. Dinh, D. Krueger, and Y. Bengio, “Nice: Non-linear independent components estimation,” *arXiv preprint arXiv:1410.8516*, 2014.
- [69] G. Papamakarios, T. Pavlakou, and I. Murray, “Masked autoregressive flow for density estimation,” *Advances in neural information processing systems*, vol. 30, 2017.
- [70] D. P. Kingma, T. Salimans, R. Jozefowicz, X. Chen, I. Sutskever, and M. Welling, “Improved variational inference with inverse autoregressive flow,” *Advances in neural information processing systems*, vol. 29, 2016.
- [71] C. Villani *et al.*, *Optimal transport: old and new*. Springer, 2009, vol. 338.
- [72] T. Karras, S. Laine, and T. Aila, “A style-based generator architecture for generative adversarial networks,” in *Proceedings of the IEEE/CVF conference on computer vision and pattern recognition*, 2019, pp. 4401–4410.
- [73] K. Zhang, W. Zuo, Y. Chen, D. Meng, and L. Zhang, “Beyond a gaussian denoiser: Residual learning of deep cnn for image denoising,” *IEEE transactions on image processing*, vol. 26, no. 7, pp. 3142–3155, 2017.
- [74] M. Ronchetti, “Torchraddon: Fast differentiable routines for computed tomography,” *arXiv preprint arXiv:2009.14788*, 2020.
- [75] L. Ardizzone, T. Bungert, F. Draxler, U. Köthe, J. Kruse, R. Schmier, and P. Sorrenson, “Framework for Easily Invertible Architectures (FrEIA),” 2018–2022. [Online]. Available: <https://github.com/vislearn/FrEIA>
- [76] J. Leuschner, M. Schmidt, D. O. Bague, and P. Maass, “Lodopab-ct, a benchmark dataset for low-dose computed tomography reconstruction,” *Scientific Data*, vol. 8, no. 1, p. 109, 2021.